

Targeting Mechanoresponsive Proteins in Pancreatic Cancer: 4-Hydroxyacetophenone Blocks Dissemination and Invasion by Activating MYH14



Alexandra Surcel¹, Eric S. Schiffhauer¹, Dustin G. Thomas¹, Qingfeng Zhu², Kathleen T. DiNapoli^{1,3}, Maik Herbig⁴, Oliver Otto⁴, Hoku West-Foyle¹, Angela Jacobi⁴, Martin Kräter⁴, Katarzyna Plak⁴, Jochen Guck⁴, Elizabeth M. Jaffee⁵, Pablo A. Iglesias^{1,3}, Robert A. Anders², and Douglas N. Robinson^{1,6,7}

Abstract

Metastasis is complex, involving multiple genetic, epigenetic, biochemical, and physical changes in the cancer cell and its microenvironment. Cells with metastatic potential are often characterized by altered cellular contractility and deformability, lending them the flexibility to disseminate and navigate through different microenvironments. We demonstrate that mechanoresponsiveness is a hallmark of pancreatic cancer cells. Key mechanoresponsive proteins, those that accumulate in response to mechanical stress, specifically nonmuscle myosin IIA (MYH9) and IIC (MYH14), α -actinin 4, and filamin B, were highly expressed in pancreatic cancer as compared with healthy ductal epithelia. Their less responsive sister paralogs—myosin IIB (MYH10), α -actinin 1, and filamin A—had lower expression differential or disappeared with cancer progression. We demonstrate that proteins whose cellular contributions are often overlooked because of their low abundance can have profound impact on cell architecture, behavior, and mechan-

ics. Here, the low abundant protein MYH14 promoted metastatic behavior and could be exploited with 4-hydroxyacetophenone (4-HAP), which increased MYH14 assembly, stiffening cells. As a result, 4-HAP decreased dissemination, induced cortical actin belts in spheroids, and slowed retrograde actin flow. 4-HAP also reduced liver metastases in human pancreatic cancer-bearing nude mice. Thus, increasing MYH14 assembly overwhelms the ability of cells to polarize and invade, suggesting targeting the mechanoresponsive proteins of the actin cytoskeleton as a new strategy to improve the survival of patients with pancreatic cancer.

Significance: This study demonstrates that mechanoresponsive proteins become upregulated with pancreatic cancer progression and that this system of proteins can be pharmacologically targeted to inhibit the metastatic potential of pancreatic cancer cells.

Introduction

Altered mechanical states of cells and tissues underlie morphologic changes concomitant with cancer progression (1–6). Cells undergo shifts in their contractility and deformability, with alterations in deformability being correlated with aggressiveness and patient outcome. Physical changes in the extracellular matrix (ECM) of the stroma and alterations in the cellular composition of tumor microenvironments are established promoters of aggressive cancer behavior (7–10). In addition, as cancer cells move from the primary tissue environment to distal locations through dissemination, invasion, and finally the establishment of metastatic niches, they experience a broad range of external environments. Thus, metastasis occurs at the interface of how a cell physically interacts with a changing mechanical landscape—these interactions are likely dependent on a cell's intrinsic adaptability to sense and respond to these mechanical changes (11). We anticipate that this cellular adaptability allows the cell to tune its mechanical state and force-generating capability as needed and depends on the cell's highly dynamic toolbox of mechanoresponsive proteins (defined here as those having the ability to redistribute in response to mechanical stress; refs. 12, 13). This toolbox, along with its regulatory components, collectively constitutes the mechanobiome.

¹Department of Cell Biology, Johns Hopkins University School of Medicine, Baltimore, Maryland. ²Department of Pathology, Johns Hopkins University School of Medicine, Baltimore, Maryland. ³Department of Electrical and Computer Engineering, Johns Hopkins University Whiting School of Engineering, Baltimore, Maryland. ⁴Biotechnology Center, Center for Molecular and Cellular Bioengineering, Technische Universität Dresden, Dresden, Germany. ⁵Department of Oncology, Sidney Kimmel Cancer Center at Johns Hopkins, The Skip Viragh Pancreatic Cancer Center, and the Bloomberg Kimmel Institute, Johns Hopkins University, Baltimore, Maryland. ⁶Department of Pharmacology and Molecular Sciences, Johns Hopkins University School of Medicine, Baltimore, Maryland. ⁷Department of Medicine, Johns Hopkins University School of Medicine, Baltimore, Maryland.

Note: Supplementary data for this article are available at Cancer Research Online (<http://cancerres.aacrjournals.org/>).

Current address for O. Otto: Centre for Innovation Competence, Humoral Immune Reactions in Cardiovascular Diseases Biomechanics, University of Greifswald, Greifswald, Germany.

Corresponding Authors: Douglas N. Robinson and Alexandra Surcel, Johns Hopkins School of Medicine, 725 N. Wolfe St., Baltimore, MD 21205. Phone: 410-502-2850; Fax: 410-955-4129; E-mail: dnr@jhmi.edu; asurcel@jhmi.edu

Cancer Res 2019;79:4665–78

doi: 10.1158/0008-5472.CAN-18-3131

©2019 American Association for Cancer Research.

The mechanobiome is the network of proteins that defines the cell's mechanical properties, generates forces, integrates chemical and mechanical cues, and feeds this information back onto other cellular processes, such as gene expression and metabolism (14–17). These proteins affect cell mechanics through active force generation that results from actin assembly that pushes outward on the membrane and myosin II-mediated contractility that pulls inward on the membrane (18). Myosin II-mediated contractility also depends on other actin crosslinking proteins in the cytoskeletal network, and their cross-talk fine-tunes the deformability and contractility of the cell (12). Unsurprisingly, this mechanical network undergoes striking changes in expression during cancer progression, which facilitates the dramatic spatial and temporal reorganization of the cytoskeleton in a metastatic cell. Varying protein levels of critical components of the mechanobiome and the broader actin cytoskeleton have been observed in a wide range of cancers (19–30). In addition, major cancer drivers and signaling proteins have altered expression patterns and additionally impact cell mechanics. Yes-Associated Protein (YAP), whose overexpression is associated with numerous cancers (31), modulates cellular actin architecture and nonmuscle myosin II regulatory light chain expression and phosphorylation, in turn affecting mechanical parameters, specifically cortical tension and deformability (32). Early activating KRAS mutations that occur in over 90% of pancreatic cancers, and at high rates in colorectal and lung cancers, lead to increased deformability and altered contractility (33, 34). Overexpression of members of the 14-3-3 family is negatively correlated with prognosis for glioblastoma (35) and liver (36), pancreatic (37), and lung (38) cancer patients. Although 14-3-3 proteins are involved in numerous biological processes, they also modulate nonmuscle myosin II bipolar filament assembly and cell mechanics (39, 40). Furthermore, a key inhibitor of myosin II, the myosin light chain phosphatase subunit MYPT1, is highly upregulated in pancreatic cancer (41).

Here we use a battery of model systems to test the concept that the upregulation of mechanoresponsive proteins may be harnessed for small molecule manipulation with the goal of returning an invasive cell to a more stable, noninvasive state (Supplementary Fig. S1). To accomplish this, we first demonstrate that mechanoresponsive proteins are upregulated in patient-derived pancreatic cancer tissue samples and cell lines, and that these proteins directly impact cell mechanics. We find that altered pancreatic ductal adenocarcinoma cancer (PDAC) mechanics emanate in part from a changing ratio of nonmuscle myosin IIs, wherein myosin IIA (MYH9) and IIC (MYH14) are upregulated, and myosin IIB (MYH10) is downregulated. We quantify the concentration of nonmuscle myosin paralogs in pancreatic cancer cells, and find that despite its relatively low concentration, myosin IIC has a significant impact on single cell behavior and collective behavior in tissue spheroids. We then demonstrate that an upregulated mechanoresponsive protein can be used as a pharmacologic target, by using a small molecule mechanical modulator, 4-hydroxyacetophenone (4-HAP), which we previously discovered increases the assembly of myosin IIC and stiffens PDAC cells (42). Since then, others have shown that 4-HAP increases the stiffness of breast cancer cells (43). We find that 4-HAP induces cortical actin belts and increases transverse actin arcs in single cells and tissue spheroids in a myosin IIC-dependent manner. This 4-HAP-induced

change in cytoskeletal structure and mechanics leads to a decrease in PDAC metastasis in a mouse liver metastasis model. In Bryan and colleagues (submitted for publication), 4-HAP also reduces metastasis in a colorectal cancer model. Thus, we collectively demonstrate that specifically targeting mechanoresponsive proteins by increasing their activity (in this case by promoting myosin IIC assembly) has therapeutic potential for patients.

Materials and Methods

Statistical analysis

Parametric and nonparametric analyses were used throughout the study. For continuous distribution data sets, we used either the Student *t* test or the Mann–Whitney Wilcoxon test for 2 groups. For multiple groups, either ANOVA followed by Fisher least square difference *post hoc* test or the Kruskal–Wallis followed by the Mann–Whitney–Wilcoxon was used. For 2 groups characterized as a frequency (percentage), we used comparison of proportions. We used KaleidaGraph (Synergy Software), R, or manual calculation. The tests used are described in individual methods sections and in figure legends. *P* values are presented either in the figure legend or figure panels.

Cell culture, cell strains, and human patient samples

Parental pancreatic cell lines. Human pancreatic ductal epithelial cells (HPDE) were obtained from Dr. Ming-Sound Tsao (University of Toronto, Ontario, Canada), and human primary tumor-derived cells (Panc10.05), human metastatically-derived cells (AsPC-1), and human-derived HeLa cells were purchased from ATCC. The Panc4.03 cell line was established in the Jaffee lab. All were grown using standard cell culture methods. HPDE cells were grown in Keratinocyte media (Gibco) with 1% penicillin and streptomycin, whereas Panc10.05, Panc02, Panc4.03, and AsPC-1 cells were grown in RPMI1640, L-glutamine media (Gibco) supplemented with 1% penicillin and streptomycin, sodium pyruvate (Gibco), nonessential amino acids (Gibco), 10% FBS (ATLAS Bio), and 0.2% insulin. HeLa cells were grown in DMEM (Gibco) with 1% penicillin and streptomycin and 10% FBS (ATLAS Bio). In accordance with NIH guidelines, cell lines were authenticated using short tandem repeat profiling at the genetic resources core facility at Johns Hopkins University. Routine *Mycoplasma* testing was performed by MycoAlert Mycoplasma Detection Kit (catalog no. LT07-118) every 3 to 6 months. Cell lines were grown for no more than 10 passages in all experiments.

IHC of patient samples. The human tissue was collected and evaluated under JHH IRB #NA_00001584. Human pancreatic cancer samples were fixed in formalin, paraffin embedded, and processed for routine histology. Additional 5- μ m sections were cut onto plus slides and baked prior to IHC staining. Details of the antibodies and methods for staining are provided in the Supplementary Materials and Methods. Quantitative analysis of tissue samples (Supplementary Fig. S2A) across stages of cancer progression (Supplementary Fig. S2B), plus expression pattern data from the Gene Expression Omnibus (Supplementary Fig. S2C) are shown in the Supplementary Information.

Engineered cell lines. Both lentiviral knockdown and adenoviral overexpression cell lines were generated in Panc10.05, and in some cases AsPC-1 and HPDE parental strains. For lentiviral

knockdown, the hairpins used (Sigma Mission shRNA) were selected after having analyzed a minimum of 3 shRNAs for each gene:

shCTRL NT control: 5'-CAACAAGATGAAGAGCACCAA-3'
 shIIA: 5'-GCCAAGCTCAAGAACAAGCAT-3'
 shIIC: 5'-GCTCAAATATGAGGCCACAAT-3'
 shACTN4: 5'-CAGGACATGTTTCATCGTCCAT-3'
 shFLNB: 5'-GCTGACATTGAAATGCCCTTT-3'

Target plasmids were cotransfected with generation 2.0 lentiviral packaging plasmids psPAX.2 and pMD2.G via Transit 20/20 (Mirrus) transfection reagent into Lenti-X HEK293t cells. Sixteen hours after transfection, the media was changed to fresh DMEM (10% FBS/1% penicillin–streptomycin). Virus-containing media was harvested after an additional 24 hours for lentiviral infection to target cells. Positively infected cells were then selected for with 1 or 5 ng/mL puromycin in Panc10.05 or AsPC-1 cells, respectively, for 5 days as determined by kill-curve analysis. Quantification of expression in control and knockdown lines was confirmed by Western blot analysis and CqPCR (Supplementary Fig. S3).

For overexpression using the adenoviral system, fluorescent adenovirus for the expression of GFP-MYH9, GFP-MYH10, MYH14-GFP, mCherry-ACTN1, GFP-ACTN4, and GFP control were purchased from Vector BioLabs. Optimal multiplicity of infection (MOI = no. of virus particles/cell) was first calculated by plating equal numbers of cells in a 96-well plate, then titrating virus between 0 and 200 MOI and observing fluorescence and cell death at 48 hours. For the myosins, the optimal MOI was found to be 50, where cell death was not seen and the percent of fluorescent cells was highest. Although an MOI of 50 showed the highest expression and no death for the α -actinin constructs, the amount of protein expressed in cells was extremely high by Western blot analysis, and so the MOI was lowered to 10. For all studies, an MOI of 50 was used for the GFP control. The filamin A and filamin B genes were too large to insert in an adenoviral vector with a fluorescent reporter. For mechanoresponse experiments on filamin A and filamin B or myosinIIC_{pep}, AsPC-1 and HeLa cells respectively were transiently transfected with FuGene HD transfection reagent (Promega) using 1 μ g of DNA for each plasmid and imaged 36 hours posttransfection. The filamin A plasmid, pmdsRed-FLNA, was a gift from Fumihiko Nakamura. The filamin B plasmid, EGFP-FLNB-pCI-C1, was a gift from Arnoud Sonnenberg. The myosinIIC_{pep} was constructed as described in the Supplementary Materials and Methods.

Experimental setup and analysis

The cell lines described above were used throughout the study across multiple experimental designs. Detailed methods for IHC with patient-derived samples (including antibodies, reagents, preparation, staining, scoring, and analysis), quantification of cellular myosin II paralog concentrations, mechanoresponse, and mechanics measurements via micropipette aspiration (MPA) and real-time deformability cytometry (RT-DC), 2D random migration, actin retrograde flow, transwell assays, tissue spheroids (generation, staining, and quantification), and mouse hemisplenectomies (IACUC protocol #M014M94) can be found in the Supplementary Materials and Methods.

Results

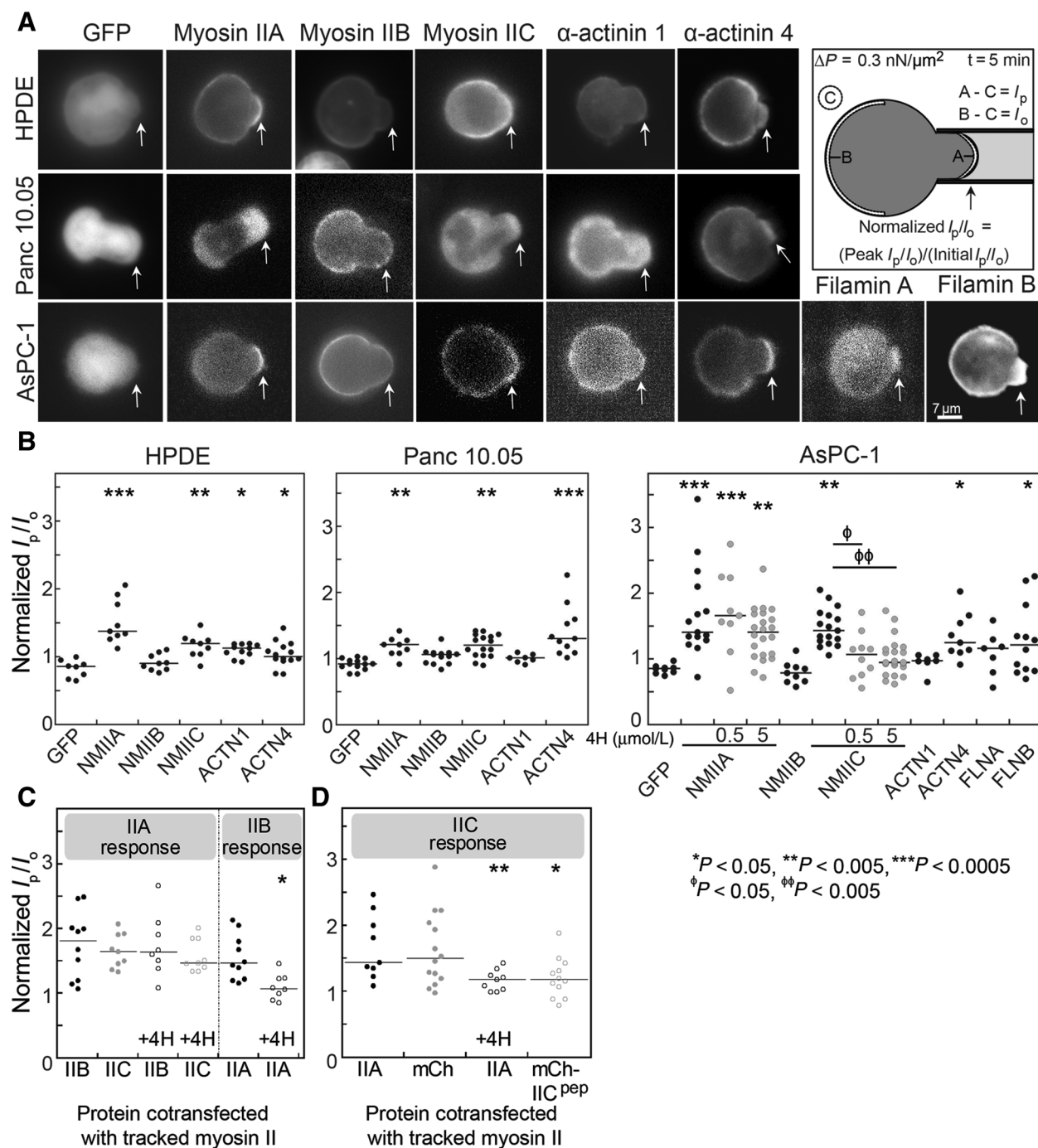
Mechanoresponsive machinery is upregulated in pancreatic cancer

Using the social amoeba *Dictyostelium discoideum*, we previously identified 10 mechanoresponsive proteins from a survey of ~35 proteins that accumulate in varying degrees to externally applied mechanical pressure (12, 44, 45). With these 10, we used mathematical modeling to develop a physical theory to explain the accumulation of 3 critical structural elements across phyla—nonmuscle myosin II, α -actinin, and filamin (12, 46). Our theory also predicted which paralogs of these proteins found in mammals were mechanoresponsive (13). To determine if these mechanoresponsive proteins have similar function in human disease, we assessed their localization in human pancreatic cancer cell lines in response to applied external stress by using MPA (Fig. 1). Fluorescently labeled myosin IIA (MYH9), IIB (MYH10), and IIC (MYH14), as well as the actin crosslinkers α -actinin 1 (ACTN1), α -actinin 4 (ACTN4), filamin A (FLNA), and filamin B (FLNB) were transiently expressed in several cell lines. These cell lines included HPDE (immortalized human pancreatic ductal epithelial cells), Panc10.05 (stage II pancreatic adenocarcinoma-derived), and AsPC-1 (stage IV ascites-metastasis-derived; Fig. 1A). Cells were deformed for 5 minutes at a pressure of 0.3 nN/ μ m², and the maximal protein accumulation in response to the dilational deformation at the aspirated tip of the cell was quantified by normalizing the fluorescence intensity at the tip region (I_p) to the unstressed cortex opposite of the pipette (I_0 ; Fig. 1B).

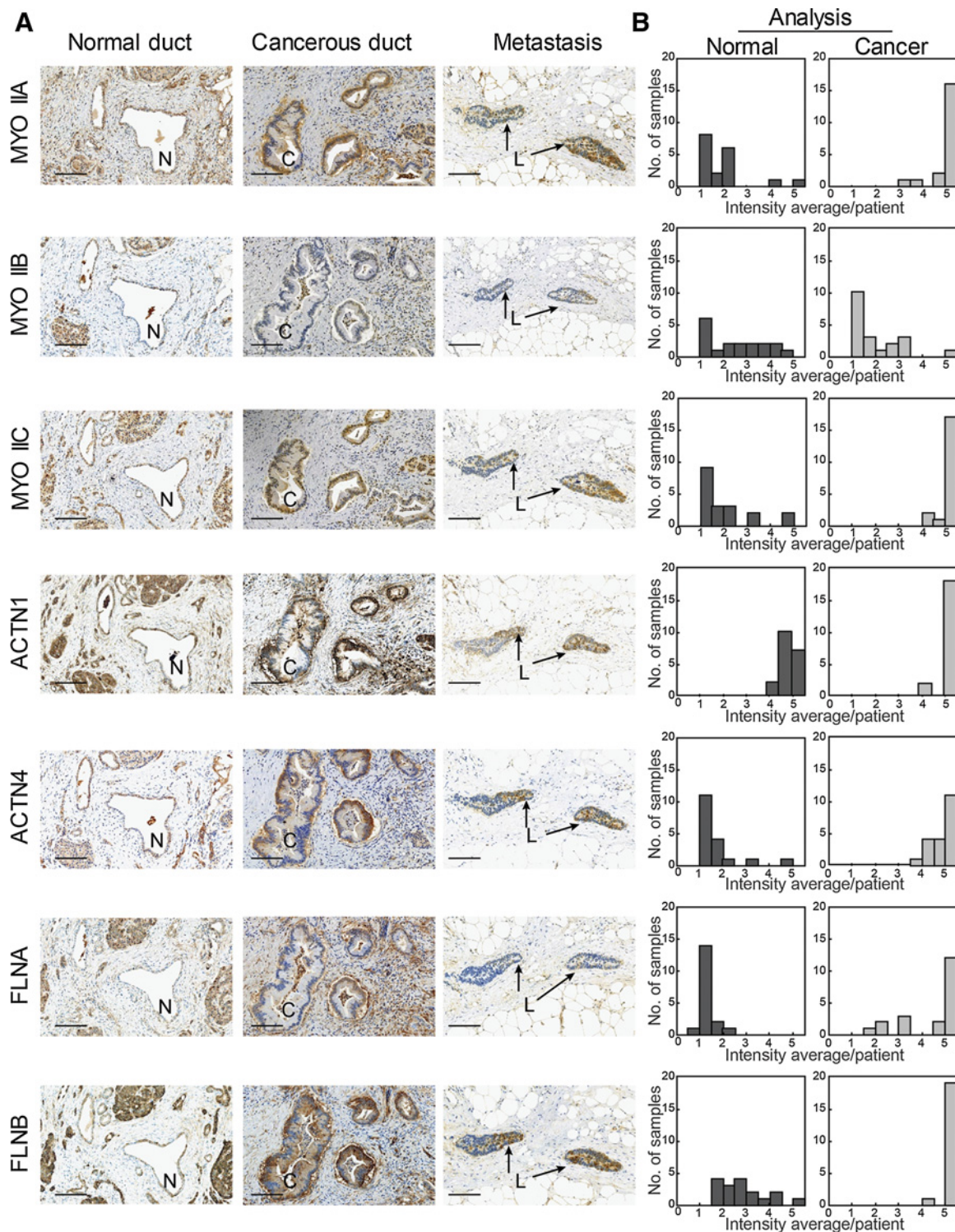
Myosin IIA and myosin IIC were mechanoresponsive in all cell lines relative to GFP-only controls, whereas myosin IIB showed no accumulation, consistent with its previously observed cell type-specific mechanoresponsiveness (Fig. 1A and B; refs. 13, 47). Because myosin IIA, IIB, and IIC can coassemble in cells (48), we then tested how the paralogs might influence each other's mechanoresponsiveness and found that each paralog's mechanoresponsiveness was independent of the other paralogs (Fig. 1C and D).

Of the α -actinins, α -actinin 4, but not α -actinin 1, was mechanoresponsive, especially in Panc10.05 and AsPC-1 cells. This differential behavior between the α -actinin paralogs likely results from the much lower actin binding affinity of the actin binding domain of α -actinin 4 ($K_d = 32 \mu$ mol/L) compared with that of α -actinin 1 ($K_d = 0.36 \mu$ mol/L). This affinity differential leads to a more dynamic α -actinin 4 behavior that is necessary for the protein to respond to mechanical stress (13). As we predicted, the scenario for filamins differs with regard to actin binding affinity because cooperativity now plays a role (12, 13). In this case, filamin B ($K_d = 7 \mu$ mol/L) showed a stronger mechanoresponse than filamin A ($K_d = 17 \mu$ mol/L) did (Fig. 1; ref. 13).

We hypothesized that the mechanoresponsive machinery is upregulated concomitant with cancer initiation and progression to endow cells with the ability to sense and respond to changing physical environments across discrete tissue types. To test this idea, we performed IHC on pancreatic cancer tissue samples from 20 patients across all 7 proteins—the 3 nonmuscle myosin IIs (IIA, IIB, and IIC), the 2 α -actinins (1 and 4), and the 2 filamins (A and B). We compared normal ducts with cancerous ducts in primary and metastatic lesions. In addition, we derived a scoring system that allowed us to delineate between high expression and low expression, as well as percentage of cells positively stained

**Figure 1.**

Nonmuscle myosin IIA, myosin IIC, α -actinin 4, and filamin B show mechanoresponsiveness in pancreatic cancer cells. **A**, Representative images across HPDE, Panc10.05, and AsPC-1 cell lines of the maximum accumulation of GFP alone, GFP-labeled myosin IIs, α -actinin 4, filamin A and filamin B, and mCherry- α -actinin 1, show peak intensity after applied stress in MPA mechanoresponse experiments. Arrows identify regions where mechanical stress was applied. Scale bar, 7 μm . Cartoon shows how mechanoresponse is calculated. **B**, Quantification of mechanoresponsiveness normalized as a ratio of fluorescence intensity at the tip (I_p) to the intensity at the opposite cortex (I_o), both in the absence of and the presence of two different concentrations of 4-HAP. **C** and **D**, Quantification of mechanoresponsiveness of myosin IIA and IIB normalized as an I_p/I_o ratio in HeLa cells cotransfected with different myosin paralogs in the presence and absence of 500 nmol/L 4-HAP. We used HeLa cells here because myosin IIB is mechanoresponsive in these cells (13, 47). **D**, In addition, quantification of myosin IIC cotransfected with a small myosin IIC peptide known to induce IIC assembly is provided. Medians plotted. *, $P < 0.05$; **, $P < 0.005$; ***, $P < 0.0005$.

**Figure 2.**

The mechanoresponsive machinery is elevated in pancreatic ductal adenocarcinoma in human pancreatic tissue. **A**, IHC staining of pancreatic tissue from human PDAC patients shows increased expression in the cancerous ducts of mechanoresponsive proteins nonmuscle myosin IIA and IIC, α -actinin 4, and both filamin A and B. Scale bar, 100 μ m. For each sample—normal duct (N), cancerous duct (C), and metastatic lesion (L)—the same site is shown across all 7 antibodies stained. In addition, both the normal and cancerous ducts are from the same patient. **B**, Quantification of staining intensity and surface area across 20 patients illustrate an upregulation of mechanoresponsive proteins, as well as filamin A. Data are plotted as a histogram of the intensity average per patient (described in Supplementary Fig. S1A and Materials and Methods) across the study group.

within the quantified ducts (outlined in Supplementary Fig. S2A). All mechanoresponsive proteins showed a significant increase in expression in cancerous versus normal ducts (Fig. 2A; Supplementary Fig. S2B), quantified in Fig. 2B. Myosin IIA and myosin IIC increased in expression, with myosin IIC specifically upregulated in the adenocarcinoma, whereas myosin IIA increased across the pancreatic cancer stroma in addition to the ducts. The non-mechanoresponsive myosin IIB showed no significant change in expression, with very little staining in both normal and cancerous pancreatic tissues. The mechanoresponsive α -actinin 4 also increased in expression in the ducts, concurrent with cancer progression, whereas α -actinin 1 maintained mostly uniform expression levels across all ducts. Filamin B, which is also highly mechanoresponsive, is upregulated specifically in cancerous ducts. In contrast, filamin A, which is much less mechanoresponsive, is upregulated across the entire pancreatic tissue, including the stroma. These patterns were also noted in noninvasive lesions, termed pancreatic intraepithelial neoplasia (PanINs; Supplementary Fig. S2B), with increasing expression associated with cancer progression. Our results are largely in keeping with normal versus pancreatic cancer tissue datasets in the Gene Expression Omnibus (GEO; Supplementary Fig. S2C). The staining patterns are also consistent with the Human Protein Atlas, which tracks RNA and IHC and which suggests that filamin B and α -actinin 4 are poor prognostic indicators for patients with pancreatic cancer (49). Filamin A shows variable PDAC expression across these studies, and α -actinin 1 displays high staining in both normal and cancerous cells. Overall, the IHC data indicate that, as a unit, the mechanoresponsive machinery is upregulated in the pancreatic ductal adenocarcinomas of patient tumors.

PDAC cell lines as a mechanoresponsive model for PDAC

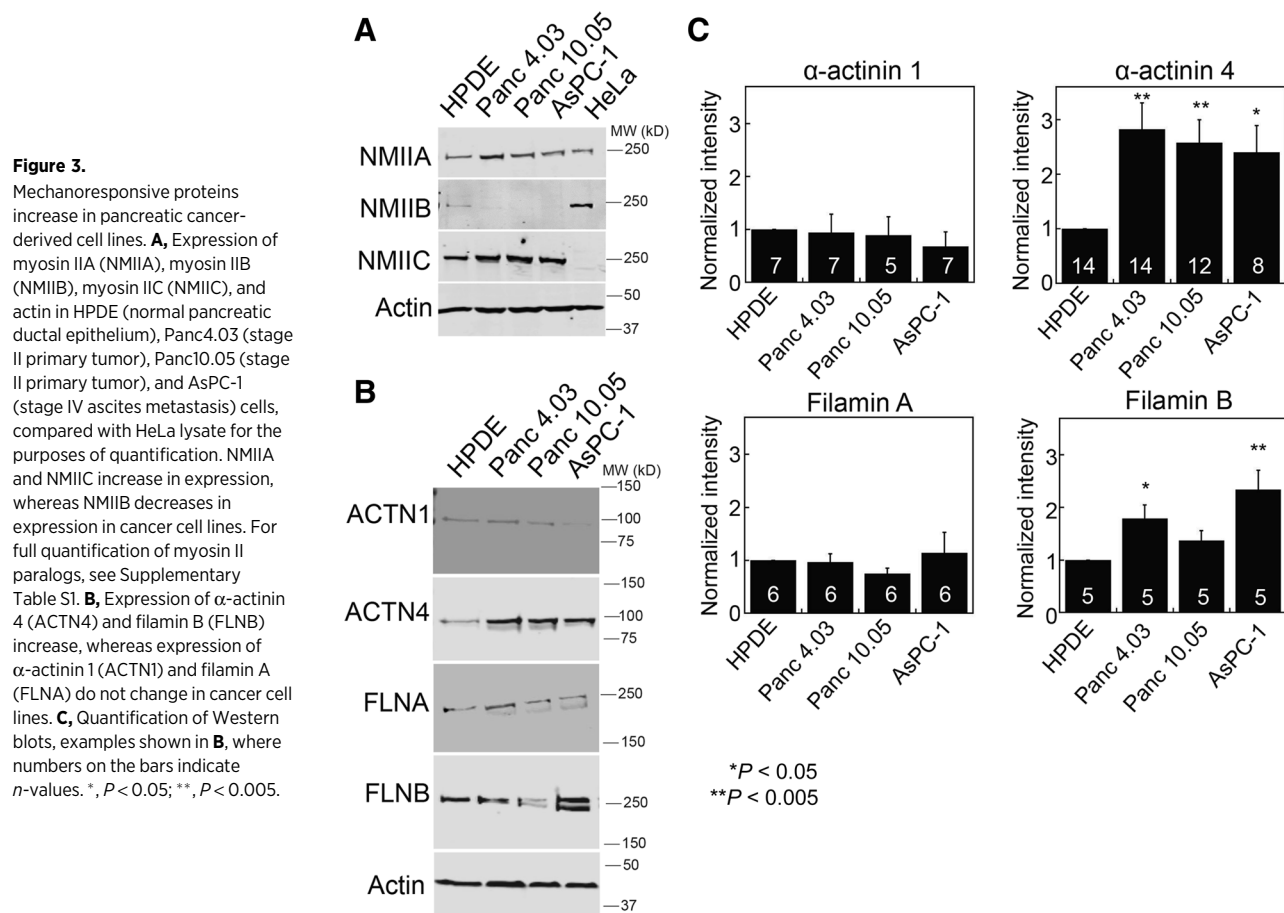
To determine if PDAC cell lines can be used to study the changing mechanobiome landscape, we first assessed if the expression patterns that we observed in patient samples (Fig. 2) matched generally with changes between wild-type (WT)-like HPDE and various primary tumor and metastatically-derived lines. Western analysis across 4 lines revealed a general increase in myosin IIA and IIC, the disappearance of myosin IIB, and an increase in α -actinin 4 and filamin B, with moderate or unchanged levels of α -actinin 1 and filamin A (Fig. 3A–C; Supplementary Table S1). To begin to develop a quantitative framework for the role of myosin IIs in pancreatic cancer, we measured the concentration of each myosin paralog in these pancreatic cancer-derived cells. We first calibrated both HeLa cells, which express myosin IIA and IIB, and AsPC-1 cells, which express myosin IIC, to generate a quantitative comparator for measuring each paralog's concentration across cell lines. To calibrate HeLa and AsPC-1 cells, we added purified paralog-specific myosin II tail fragments to the extract (Supplementary Fig. S3A). From these calibration measurements, we calculated that the nonmuscle myosin IIA concentration in human pancreatic cells ranged from 540 nmol/L in HPDE cells to 770 nmol/L in Panc4.03 cells. These values compare favorably with the amounts of myosin II in budding yeast (Myo2p, 450 nmol/L; Myp2p, 380 nmol/L; ref. 50) and in *Dictyostelium discoideum* (Myo II, 3.4 μ mol/L; Supplementary Table S1; ref. 51). By comparison to myosin IIA, myosin IIB and IIC are found at much lower concentrations. Interestingly, myosin IIC increased 1.5-fold from approximately 2% of all myosin II in HPDE cells to about 3% of all myosin II in AsPC-

1 cells, whereas myosin IIB decreased from ~8% of all myosin II in HPDEs to undetectable in AsPC-1 cells (Fig. 3A; Supplementary Table S1). The dramatic change in myosin IIC in normal and cancerous ducts in the immunohistochemistry is consistent with the myosin quantification across PDAC cell lines (Fig. 2). Myosin IIC also exists in 2 splice variants, and we find that both variants increase in expression in AsPC-1 cells (Supplementary Fig. S3B). Although myosin IIC appears to be a minor myosin II paralog based on its concentration, in fact we find below that this paralog plays a major role in pancreatic cancer cell mechanics and behavior.

Modulation of cell mechanics through mechanoresponsive machinery and 4-HAP

We previously demonstrated that WT-like HPDE cells are less deformable than patient-derived PDAC cell lines (42). To determine if mechanoresponsive elements of the PDAC mechanobiome contribute to this mechanical differential, we used MPA to measure the effective cortical tension (T_{eff}) of cells with overexpression or knockdown of myosin II, α -actinin, and filamin paralogs in Panc10.05 cells (Fig. 4A; Supplementary Fig. S3A, S3C, S3D, and S3E). Across all cell lines, knockdowns were 70% to 95% (Supplementary Fig. S3C and S3E). Driving myosin IIA levels up or down yielded an altered cortical tension, which rose and fell with myosin IIA expression levels. Myosin IIB overexpression had no impact on cortical tension. Myosin IIB knockdowns were not pursued since Panc10.05 cells (as well as other PDAC lines and patient tissue samples) have no detectable levels of this protein (Fig. 2A and Fig. 3A; Supplementary Fig. S2). α -actinin 1 overexpression had no effect on cell mechanics, whereas both overexpression and knockdown of α -actinin 4 decreased the T_{eff} by half (Fig. 4A; Supplementary Fig. S3C, S3D, and S3E). Filamin A and B overexpressing cells ruptured under the applied pressures needed to measure cortical tension where the condition of $L_p = R_p$ must be met. However, filamin B knockdown cells could be measured and had an increase in cortical tension (Fig. 4A).

Interestingly, despite contributing only 3% of the overall myosin II in these cells (Supplementary Table S1), overexpression and knockdown of myosin IIC had a profound impact on cell mechanics, leading to an overall reduction in cortical tension of 20% and 40%, respectively (Fig. 4A). Myosin IIC has a similar impact on mechanics in colorectal cancer cells, where it also constitutes a small percentage of the total myosin II (Bryan and colleagues, submitted for publication). To further explore the impact that myosin IIC has on the PDAC mechanobiome and cell mechanics, we used the small molecule 4-HAP, which we previously identified in a *Dictyostelium* screen for mechanical modulators. In *Dictyostelium*, 4-HAP increased cortical tension by driving myosin II to the cell cortex. 4-HAP shows myosin II-paralog specificity in mammalian cells by increasing the assembly of myosin IIC (and IIB) and decreasing the deformability of several PDAC cell lines (42). Indeed, 4-HAP treatment increased the cortical tension of control cells where myosin IIC is present, but had no impact on myosin IIC-depleted cells (Fig. 4A). In addition, 4-HAP also extinguished the mechanoresponsiveness of myosin IIC in a dose-dependent manner, with no effect on myosin IIA mechanoresponsiveness (Fig. 1B). We also confirmed that 4-HAP treatment did not alter expression of the myosin II paralogs over a 24-hour window (Supplementary Fig. S3F).



Knowing that the myosin II paralogs' mechanoresponsiveness was independent of each other (Fig. 1C and D), we tested how they might influence 4-HAP's ability to inhibit myosin IIC's mechanoresponse. The overexpression of myosin IIB or IIC did not affect myosin IIA's mechanoresponsiveness, even in the presence of 4-HAP (Fig. 1C). However, myosin IIB and myosin IIC's mechanoresponsiveness was still inhibited by 4-HAP even though myosin IIA was coexpressed with them (Fig. 1C and D). Furthermore, loss of myosin IIA does not alter myosin IIC's ability to assemble in cells, as assessed by sedimentation (Supplementary Fig. S3G).

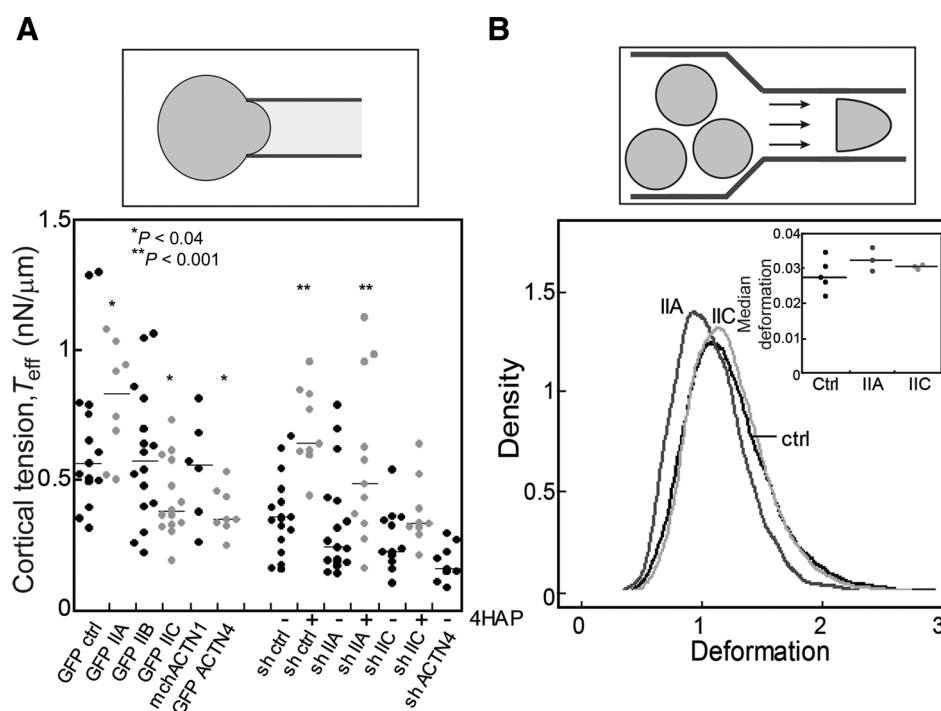
Our previous studies indicated that 4-HAP works by promoting assembly of myosin IIC and IIB (42). To further flesh out the concept that 4-HAP inhibits mechanoresponsiveness by driving overassembly of myosin IIC, we asked whether driving assembly of myosin IIC in a different manner would also inhibit its mechanoresponsiveness. To do this, we expressed the human version of the myosin IIC tail fragment that corresponds to the mouse version, known to promote bipolar filament assembly (52). Indeed, expression of the myosin IIC tail fragment inhibited myosin IIC's mechanoresponsiveness phenocopying 4-HAP's effect (Fig. 1D). These observations further confirm that 4-HAP influences myosin IIC, and myosin IIB, independently of myosin IIA and does so by promoting bipolar filament assembly.

In concert with MPA, which measures mechanical properties on the >500 milliseconds time-scale (cortical tension measurements

are performed over 10s of seconds), we used RT-DC (53), which measures mechanics on the 4-milliseconds timescale and across the whole cell (Supplementary Fig. S4A). Reduction of myosin IIA, but not myosin IIC, increased cell deformation (Fig. 4B). The deformation was converted to an elastic modulus and calculated to be 1.17 ± 0.37 kPa (mean \pm SD) for control, 1.07 ± 0.3 kPa for shIIA, and 1.21 ± 0.34 kPa for shIIC. This trending reduction (9%) in the elastic modulus measured for knockdown of myosin IIA, which is the most abundant paralog in the PDAC cells, is similar to the reduction in elasticity measured for WT versus *myoII* genetic deletion cells in *Dictyostelium* (54). The elastic modulus measured on short time-scales contrasts with the \sim 2-fold difference in cortical tension measured over longer time-scales, highlighting the complexity of the mechanical roles of these proteins (55). In addition, RT-DC revealed mechanical differences across pancreatic cancer cell lines (Supplementary Fig. S4B).

Myosin IIC alters actin bundling and flow, facilitating dissemination

In addition to mediating mechanoresponsiveness (Fig. 1) and cell mechanics (Fig. 4), nonmuscle myosin II proteins also impact cytoskeletal arrangements and contractility. To determine how myosin IIC specifically impacts the cytoskeletal organization in collectives of cells, we generated tissue spheroids with knockdown Panc10.05 cell lines and examined the impact of 4-HAP treatment on those spheroids. Control knockdowns plated in 3D collagen I matrices showed partial dissemination, which was greatly

**Figure 4.**

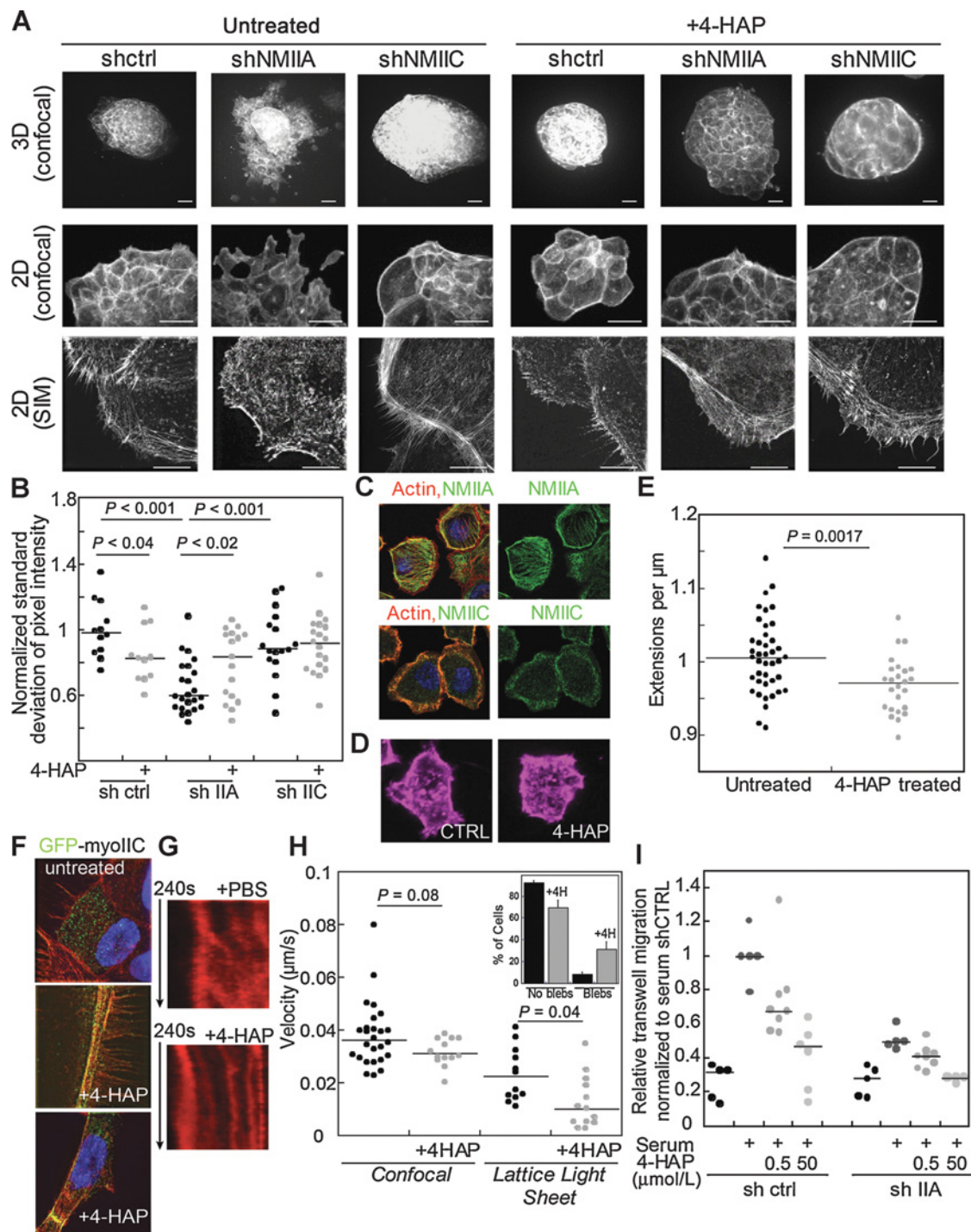
Mechanoresponsive proteins impact cortical tension and deformability of PDAC cells. **A**, The effective cortical tension (T_{eff}) measured by MPA experiments (schematic) is significantly affected by overexpression of myosin IIA, myosin IIC, and α -actinin 4, all mechanoresponsive paralogs. Five hundred nmol/L 4-HAP increased the cortical tension of sh-control cells. 4-HAP also increased the cortical tension in myosin IIA knockdown cells, whose primary myosin paralog myosin IIC was activated by 4-HAP (42). Knockdown of myosin IIC also led to a decrease in cortical tension, unchanged by 4-HAP challenge. Medians plotted. *, $P < 0.04$; **, $P < 0.0001$, relative to control. **B**, RT-DC experiments (schematic) demonstrated increased deformation when myosin IIA and myosin IIC were knocked down (plotted as a probability distribution). All cell lines were generated from Panc10.05 cells. $N = 7521$ cells for control, 9,632 cells for myosin IIA knockdown, and 5,933 cells for myosin IIC knockdown. Cell types were distinct ($P < 0.0001$). Inset, median deformation of 3 to 5 RT-DC independent runs across cell types from which the elastic modulus was calculated. Average median deformation values were 0.027 ± 0.002 (mean \pm SD) for ctrl, 0.032 ± 0.002 for IIA knockdown, and 0.031 ± 0.0003 for IIC knockdown.

increased in NMIIA knockdowns, similar to observations in other cancer models (56–58). In contrast, knockdown of myosin IIC showed no dissemination (Fig. 5A, top row). Upon treatment with 4-HAP for 24 hours, dissemination in both the control and NMIIA knockdown decreased, whereas no change was observed in the myosin IIC-depleted spheroids. To further analyze the fine-detail in cytoskeletal structures, spheroids were plated on collagen I-coated 2D substrates, and similar morphological differences were observed as in the 3D cultures (Fig. 5A, middle row). In addition, we observed tight actin cortical banding patterns on the periphery of the tumor spheroids in the absence of myosin IIC. This banding pattern was also observed in the control and NMIIA knockdown spheroids with 4-HAP treatment. To assess the actin redistribution, we used computer-assisted image analysis on the 2D spheroids and measured the continuity of banding, the percent coverage of actin filaments at the spheroid edge, and the homogeneity of the actin in those structures (calculated as the standard deviation of pixel intensity normalized to control; Supplementary Fig. S5). Across all analyses, myosin IIA knockdown spheroids had the least amount of discrete and continuous banding (Fig. 5B; Supplementary Figs. S5A and S5B) and the least amount of actin staining at the tissue edge (Supplementary Fig. S5C). Upon 4-HAP treatment, all of these metrics changed—more discrete and continuous belts emerged and the median percentage staining of actin increased 2-fold. By comparison,

the myosin IIC knockdown tissue spheroids had discrete and continuous actin belts that remained unchanged upon 4-HAP addition (Fig. 5B; Supplementary Figs. S5B and S5C), consistent with 4-HAP working primarily through myosin IIC. Interestingly, by these analytics, treatment with 4-HAP in the control tissue spheroids seemed to decrease discrete band formation.

We then used structural illumination microscopy (SIM) to acquire higher resolution views of the structures along the tissue spheroid edges (Fig. 5A, bottom row, and B). In the control spheroids, the actin belts are formed by the structural rearrangement of the actin bundles. Specifically, 4-HAP induces a coarser distribution of actin composed of dense actin belts and leads to the emergence of filopodial-like structures or retraction fibers. In the myosin IIA knockdowns treated with 4-HAP, tight actin belts, as well as elaborate arrays of parallel actin bundles, are also clearly visible. In contrast, myosin IIC knockdowns had elaborate peripheral actin structures that were largely unchanged between untreated and 4-HAP-treated samples. Thus, 4-HAP induces alterations in peripheral actin structures in a myosin IIC-dependent manner.

To address myosin IIC's role in actin rearrangements, we next determined its cellular localization. In tissue spheroids, fluorescently-labeled myosin IIC is both diffusely localized throughout the cell and along actin filaments (Fig. 5C). When actin filaments collapse to form actin belts upon 4-HAP

**Figure 5.**

Myosin IIC alters cytoskeletal actin architecture and cell behavior upon 4-HAP treatment. **A**, Panc10.05 tissue spheroids grown, stained with phalloidin, and imaged in 3D (Matrigel) or 2D (collagen) show dissemination, exacerbated in myosin IIA knockdown. Myosin IIC depletion suppresses dissemination and generates actin cortical belts. 4-HAP induces actin belts in control and myosin IIA-depleted spheroids. These belts are already present in myosin IIC-depleted spheroids. Scale bar, 40 μm (confocal) and 10 μm (SIM). **B**, Quantification of these actin structures using normalized SD of pixel intensity; see Materials and Methods. Medians plotted; P values on graphs. **C**, Endogenous myosin IIA in AsPC-1 cells localizes on actin stress fibers; myosin IIC localizes to the actin cortex. **D**, 4-HAP reduces the number of extensions formed by AsPC-1 cells. **E**, Numbers of extensions/ μm of perimetric distance are plotted. **F**, GFP-myosin IIC decorates actin filaments, especially actin belts induced by 4-HAP in tissue spheroids. **G**, Sample kymographs of line scans across active leading edges in AsPC-1 SirAct live-stained cells. **H**, 4-HAP decreases retrograde flow. Medians are plotted. Inset shows increase in bleb formation in 4-HAP-treated cells ($P = 0.0028$). **I**, AsPC-1 shCTRL and shIIA cells show dose-dependent reduction of transwell migration upon 4-HAP treatment. Medians are shown.

treatment, myosin IIC shows strong colocalization with those belts. In single Panc10.05 and AsPC-1 cells, endogenous myosin IIC is predominately confined to the cell cortex including in actin-rich protrusions, whereas myosin IIA localizes along stress fibers (Fig. 5C). In single cells, 4-HAP decreases the number of actin-rich protrusions, as measured with our edge detection algorithm (Fig. 5D and E; Supplementary Fig. S6). Similarly, in tissue spheroids, 4-HAP-induced peripheral actin belts that are rich in myosin IIC (Fig. 5F).

Overall, this analysis highlights 2 major findings. First, in collections of cells, despite being present in small quantities, myosin IIC plays a major role in mediating actin network structural rearrangements and dynamics. Myosin IIA, known to contribute to retrograde actin flow, may work in concert with myosin IIC to drive these cytoskeletal rearrangements. Second, 4-HAP reduces the fluidity of the network: by stabilizing actin belt structures in a manner independent of myosin IIA, but dependent on myosin IIC. Thus, by altering the actin cytoskeleton, 4-HAP inhibits dissemination from tissue spheroids.

Because retrograde flow moves actin filaments away from the cell perimeter, we hypothesized that the cortical actin belts could be formed by a reduction in this flow. Therefore, we examined the impact of 4-HAP on retrograde actin flow by staining live cells with SiR-actin and observing the actin network using lattice light sheet microscopy (Supplementary Fig. S6A) and confocal microscopy. Most 4-HAP-treated cells had undetectable levels of actin flow, as observed by Kymograph (Fig. 5G; Supplementary Fig. S6B). Those cells in which retrograde flow could be measured showed a 50% reduction in velocity over untreated controls (Fig. 5H; Supplementary Movies S1 and S2). In addition, cells treated with 4-HAP showed an increase in bleb formation (Fig. 5H, inset). This large and measurable impact on actin dynamics explains in part the dose-dependent decrease on trans-well migration in control and myosin IIA knockdown AsPC-1 cells (Fig. 5I). Overall, 4-HAP's reduction of actin flow, cell dissemination, and invasion indicates its potential for preventing PDAC metastasis.

4-HAP decreases PDAC metastatic potential in mice

Critical regulators of myosin II have significantly altered expression associated with pancreatic cancer progression and in pancreatic cancer-derived cell lines (19, 39, 41). These genetic alterations suggest that myosin II, particularly myosin IIC whose expression is specifically elevated in malignant pancreatic ductal epithelia, may be an attractive target for modulating PDAC cell

behavior. Therefore, we tested 4-HAP in a mouse model of PDAC using hemisplenectomy, which simulates the metastatic process to the liver. In this model, the spleen is separated into halves and tumor cells are injected into one half, which is then removed after the tumor cells have entered the liver to prevent local injection-site tumor formation. Mice develop micrometastases in 1 to 2 weeks and gross disease by 3 to 4 weeks. Athymic *NCr-nu/nu* mice with AsPC-1 liver metastases were divided into 3 groups: control (untreated), PBS (200 μ L PBS i.p. injections, every other day), and 4-HAP (5 mg/mL, 200 μ L i.p. injections, every other day). Mice were sacrificed at 5 weeks postsurgery, when the first mouse expired. Metastases to the liver were observed and quantified using our custom Matlab script, which measures surface area tumor coverage (Fig. 6A). Results from both liver weights and tumor coverage show that 4-HAP treatment led to a 50% reduction in tumor formation (Fig. 6B; Supplementary Fig. S7).

Discussion

A cell's ability to react to changing mechanical and chemical cues in its environment depends on the adaptability of its mechanobiome. Increased contractility and altered deformability, as well as rapid turnover of cytoskeletal proteins, are trademarks of cells responding to constantly changing surroundings. Gene expression programs are upregulated to provide cells with added adaptability at specific time points in developing embryos, and differentiating cells show increased expression of mechanoresponsive proteins during mechanically turbulent periods. For example, filamin's mechanoresponsiveness is required for maturation of actin-rich ring canals that interconnect the nurse cells and oocyte in developing *Drosophila* egg chambers (59), and filamin B is upregulated in embryonic vascular endothelial cells (60). Both α -actinin 1 and α -actinin 4 show temporally defined expression in developing zebrafish embryos, with both expressed in the notochord and α -actinin 4 also expressed in the developing gut (61). Each of the nonmuscle myosin II paralogs have roles in development as well, including but not limited to neurite outgrowth and maturation (NMIIB and NMIIIC; ref. 62), nephron development (NMIIA and NMIIIB; ref. 63), and hearing (NMIIA; ref. 64).

In the mechanobiome, forces are shared between myosin II and different actin crosslinkers, with myosin II having potentiating or inhibitory effects on certain crosslinkers and vice versa (12, 54). This mechanosensory system constitutes a control system, where mechanical inputs can be converted to signaling outputs in a

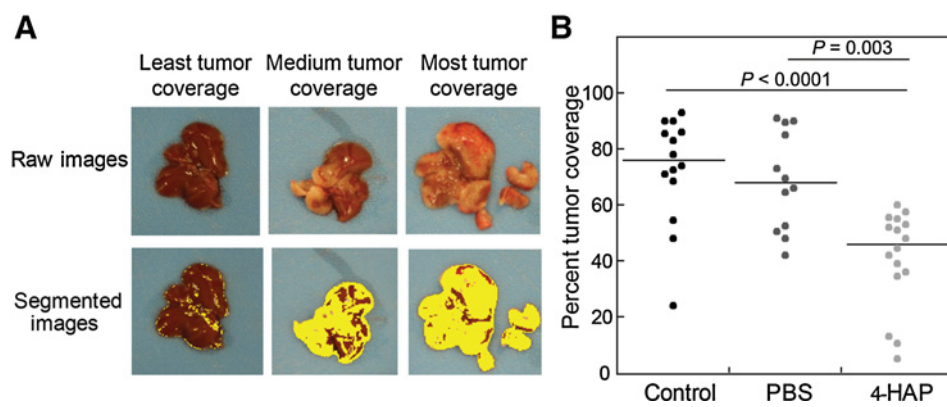
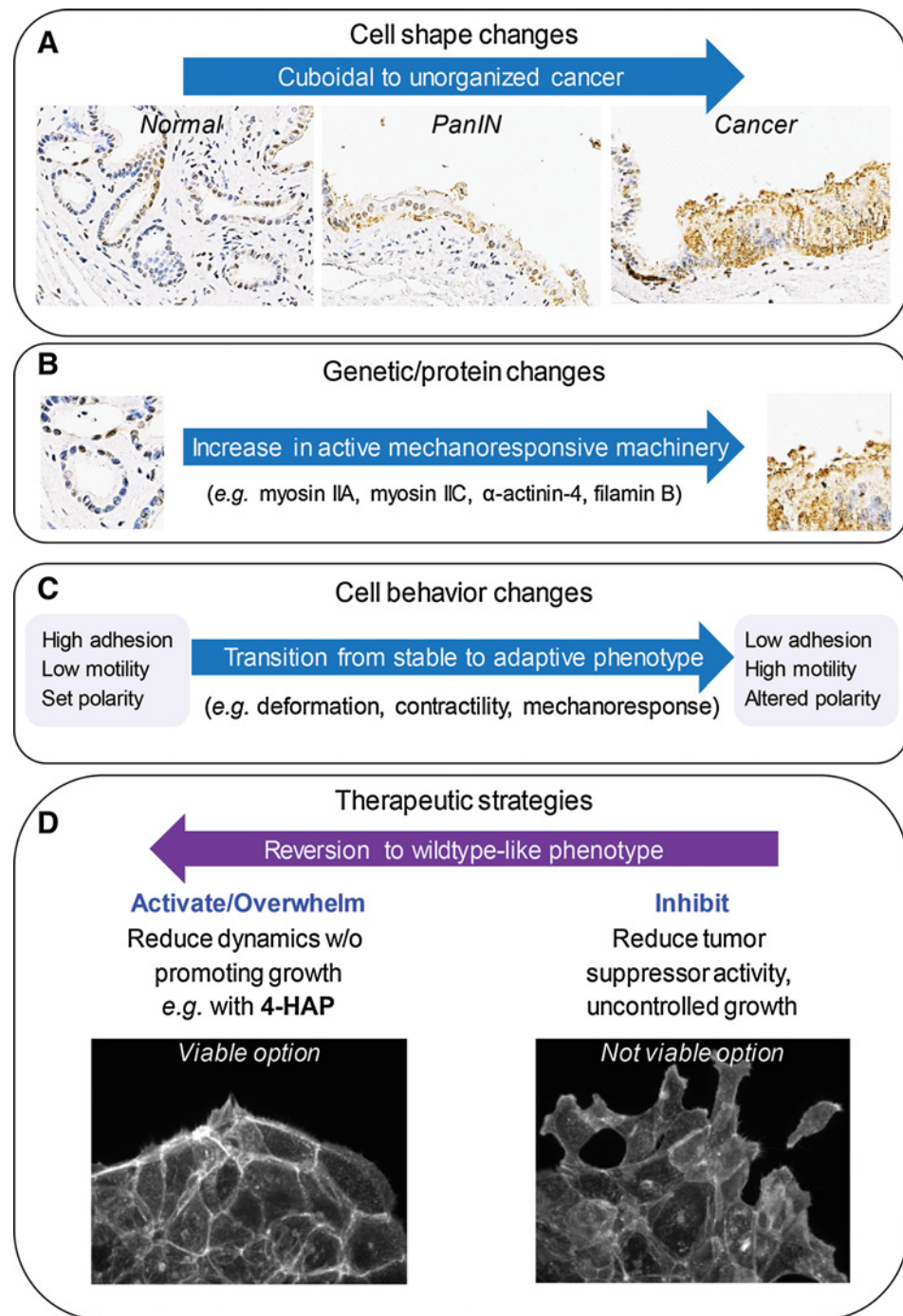


Figure 6. 4-HAP reduces PDAC liver metastasis in murine model. Livers harvested from 4-HAP-treated mice that underwent hemisplenectomies with AsPC-1 cells show a reduction in tumor coverage over those livers from untreated mice. **A**, Images were quantified using image segmentation based on color gradients to discern tumor coverage (Supplementary Fig. S5). **B**, Quantification of tumor coverage show a 50% reduction in surface tumor load. Medians are provided on the graph.

Figure 7.

New therapeutic strategy: ablate metastasis by overwhelming intrinsic machinery to prevent polarization. **A**, Pancreatic cancer progression is histologically defined by a series of cell shape change events from cuboidal epithelial cells (normal), through pseudo-stratified epithelial layers (PanIN), to disorganized and proliferic cell growth (cancer). **B**, These changes are concomitant with genetic lesions and alterations in protein expression, including those proteins that define the mechanoresponsive machinery in PDAC, primarily myosin IIA, myosin IIC, α -actinin-4, and filamin B. **C**, These changes in mechanoresponsive machinery have significant implications on cell behavior, moving the system from a stable state with high cellular adhesion, low motility, and set polarity to an adaptive state with low adhesion, high motility, and altered polarity. **D**, Common therapeutic approaches have primarily involved inhibiting key proteins. This loss of activity is not a viable approach for the PDAC mechanobiome because it leads to uncontrolled growth and dissemination as seen in myosin IIA inhibition or knockdown. Instead, we propose activating or overwhelming the system with mechanical modulators such as 4-HAP, which revert the system to a more WT-like phenotype, reducing the dynamics of the system without promoting uncontrolled growth.



manner analogous to chemical signal transduction (45). Through our work (12), an important delineation has emerged: the cell has at least 2 systems of proteins that when depleted, lead to alterations in cortical viscoelasticity and tension. One set of proteins leads to increased mechanoresponsiveness, whereas the other set of proteins leads to reduced mechanoresponsiveness. Cells that mature into terminally differentiated tissues often readjust the cytoskeletal milieu to favor reduced mechanoresponsiveness over their developmental program. These stable expression patterns, however, are altered in precancerous cells (often caused by

upstream genetic lesions), and revert cells to programs activated in early development that endow them again with increased adaptability. In fact, supporting cells of the tumor, the pancreatic stellate cells, also become highly adaptable, a trait that can be targeted to reduce tumor cell invasion (8).

The mechanobiome of the cancerous ductal cells plays an essential role in cell shape change, leading to PDAC invasion and metastasis (Fig. 7A). Specifically, the mechanoresponsive proteins myosin IIA, myosin IIC, α -actinin 4, and filamin B are upregulated in patient-derived tissues (Fig. 7B), where they alter

the structural arrangement of the actin cytoskeleton and impact cell mechanics to facilitate metastasis (Fig. 7C). In addition, despite its low abundance, myosin IIC plays an important role in facilitating actin organization and retrograde flow. Also, our data on myosin IIC suggest that changes in the expression level of minor proteins that are often discounted in larger data mining may in fact, be worthy of reconsideration, given the large impact myosin IIC has on cell mechanics and cell behavior. Our *in vivo* metastasis assays demonstrate that the myosin IIA to IIC dynamic can be fine-tuned towards a therapeutic benefit with mechanical modulators such as 4-HAP (Fig. 7D). In addition, because myosin IIC is specifically upregulated in ductal adenocarcinoma cells, the pharmacologic modulation of this protein is unlikely to negatively impact healthy pancreatic tissue; 4-HAP should synergize with other strategies such as immunological intervention in pancreatic cancer patients, since immune cells do not typically express myosin IIC (42). In fact, enhanced activation of T cells on stiffer substrates suggests that 4-HAP, which stiffens the immunological target cells, could behave as an excellent immunotherapy adjuvant (65).

In summary, the observations presented here imply that targeting cancer by broadening strategies to include small molecule mechanical modulators can have significant effects by reducing metastatic potential. Modulation of mechanoresponsive proteins has several advantages. First, we can fine-tune the activity of proteins that are upregulated in cancerous tissue, thus harnessing the cell's intrinsic protein make-up to revert them to more normal phenotypes, while protecting healthy cells that do not upregulate these targeted proteins. Second, this strategy draws upon the normal biochemistry of the protein to overwhelm the mechanics of the system. In our studies, we are hitting on both concepts: We are using 4-HAP to increase the assembly of myosin IIC, which is specifically upregulated in PDAC, in order to overcome the protein's innate adaptive ability. 4-HAP treatment pushes myosin IIC to lock onto the cytoskeletal network, thus inhibiting the tumor cell's ability to polarize and reorganize its actin cytoskeleton. This concept is reinforced by the actin structural remodeling observed in colorectal cancer cells presented in our companion paper by Bryan and colleagues (submitted for publication). Overall, incorporating the mechanobiome as a targetable drug space in combination with other therapeutic approaches is a valuable strategy for reducing PDAC metastases (Fig. 7).

References

- Remmerbach TW, Wottawah F, Dietrich J, Lincoln B, Wittekind C, Guck J. Oral cancer diagnosis by mechanical phenotyping. *Cancer Res* 2009;69:1728–32.
- Cross SE, Jin YS, Rao J, Gimzewski JK. Nanomechanical analysis of cells from cancer patients. *Nat Nanotechnol* 2007;2:780–3.
- Staunton JR, Doss BL, Lindsay S, Ros R. Correlating confocal microscopy and atomic force indentation reveals metastatic cancer cells stiffen during invasion into collagen I matrices. *Sci Rep* 2016;6:19686.
- Suresh S. Biomechanics and biophysics of cancer cells. *Acta Biomater* 2007;3:413–38.
- Kim TH, Gill NK, Nyberg KD, Nguyen AV, Hohlbauch SV, Geisse NA, et al. Cancer cells become less deformable and more invasive with activation of beta-adrenergic signaling. *J Cell Sci* 2016;129:4563–75.
- Nguyen AV, Nyberg KD, Scott MB, Welsh AM, Nguyen AH, Wu N, et al. Stiffness of pancreatic cancer cells is associated with increased invasive potential. *Integr Biol (Camb)* 2016;8:1232–45.
- Kai F, Drain AP, Weaver VM. The Extracellular Matrix Modulates the Metastatic Journey. *Dev Cell* 2019;49:332–46.
- Chronopoulos A, Robinson B, Sarper M, Cortes E, Auernheimer V, Lachowski D, et al. ATRA mechanically reprograms pancreatic stellate cells to suppress matrix remodelling and inhibit cancer cell invasion. *Nat Commun* 2016;7:12630.
- Laklai H, Miroshnikova YA, Pickup MW, Collisson EA, Kim GE, Barrett AS, et al. Genotype tunes pancreatic ductal adenocarcinoma tissue tension to induce matricellular fibrosis and tumor progression. *Nat Med* 2016;22:497–505.
- Chronopoulos A, Lieberthal TJ, Del Río Hernandez AE. Pancreatic cancer: a mechanobiology approach. *Converg Sci Phys Onc* 2017;3. doi: 10.1088/2057-1739/aa5d1b.
- Discher DE, Janmey P, Wang YL. Tissue cells feel and respond to the stiffness of their substrate. *Science* 2005;310:1139–43.
- Luo T, Mohan K, Iglesias PA, Robinson DN. Molecular mechanisms of cellular mechanosensing. *Nat Mater* 2013;12:1064–71.
- Schiffhauer ES, Luo T, Mohan K, Srivastava V, Qian X, Griffis ER, et al. Mechanoaccumulative elements of the mammalian actin cytoskeleton. *Curr Biol* 2016;26:1473–9.

Disclosure of Potential Conflicts of Interest

O. Otto is a Chief Scientific Officer at Zellmechanik Dresden. Elizabeth M. Jaffee reports receiving a commercial research grant from Aduro Biotech, Bristol Myer Squibb, and Amgen, has ownership interest (including stock, patents, etc.) for Aduro Biotech, and is a consultant/advisory board member of CSTONE, Genoea, Adaptive Biotech, and DragonFly. No potential conflicts of interest were disclosed by the other authors.

Authors' Contributions

Conception and design: A. Surcel, E.S. Schiffhauer, E.M. Jaffee, R.A. Anders, D.N. Robinson

Development of methodology: A. Surcel, E.S. Schiffhauer, D.G. Thomas, Q. Zhu, K.T. DiNapoli, O. Otto, P.A. Iglesias, R.A. Anders, D.N. Robinson

Acquisition of data (provided animals, acquired and managed patients, provided facilities, etc.): A. Surcel, E.S. Schiffhauer, D.G. Thomas, Q. Zhu, M. Herbig, O. Otto, H. West-Foyle, A. Jacobi, M. Kräter, K. Plak, R.A. Anders

Analysis and interpretation of data (e.g., statistical analysis, biostatistics, computational analysis): A. Surcel, E.S. Schiffhauer, D.G. Thomas, Q. Zhu, K.T. DiNapoli, M. Herbig, A. Jacobi, M. Kräter, E.M. Jaffee, P.A. Iglesias, R.A. Anders, D.N. Robinson

Writing, review, and/or revision of the manuscript: A. Surcel, E.S. Schiffhauer, Q. Zhu, K.T. DiNapoli, M. Kräter, J. Guck, E.M. Jaffee, R.A. Anders, D.N. Robinson

Administrative, technical, or material support (i.e., reporting or organizing data, constructing databases): A. Surcel

Study supervision: A. Surcel, J. Guck, D.N. Robinson

Acknowledgments

We thank Dr. Marc Edwards for assistance in image acquisition, Dr. Christoph Herold of TU Dresden for assistance with RT-DC, members of the Jaffee lab for helpful conversations on mouse *in vivo* studies, and members of the Robinson lab for helpful conversations over the course of this project, especially Jennifer Nguyen for help with R. This work was supported by the NIH (GM66817 and GM109863 to D. Robinson, A. Surcel, E. Schiffhauer, D. Thomas), the Sol Goldman Foundation (to A. Surcel, D. Robinson), a Johns Hopkins Discovery Grant (to D. Robinson, Q. Xu, K. DiNapoli, E. Jaffee, P. Iglesias, R. Anders), and the Alexander-von-Humboldt Foundation (AvH Professorship to J. Guck, M. Herbig, O. Otto, A. Jacobi, M. Kräter, K. Plak).

The costs of publication of this article were defrayed in part by the payment of page charges. This article must therefore be hereby marked *advertisement* in accordance with 18 U.S.C. Section 1734 solely to indicate this fact.

Received October 4, 2018; revised June 11, 2019; accepted July 22, 2019; published first July 29, 2019.

14. Torrino S, Roustans FR, Kaminski L, Bertero T, Pisano S, Ambrosetti D, et al. UBT1D1 is a mechano-regulator controlling cancer aggressiveness. *EMBO Rep* 2019;20. doi: 10.15252/embr.201846570.
15. Broders-Bondon F, Nguyen Ho-Bouldoires TH, Fernandez-Sanchez ME, Farge E. Mechanotransduction in tumor progression: the dark side of the force. *J Cell Biol* 2018;217:1571–87.
16. Salvi AM, DeMali KA. Mechanisms linking mechanotransduction and cell metabolism. *Curr Opin Cell Biol* 2018;54:114–20.
17. Kassianidou E, Kalita J, Lim RYH. The role of nucleocytoplasmic transport in mechanotransduction. *Exp Cell Res* 2019;377:86–93.
18. Schiffhauer E, Robinson DN. Mechanochemical signaling directs cell-shape change. *Biophys J* 2017;112:207–14.
19. Jones S, Zhang X, Parsons DW, Lin JC, Leary RJ, Angenendt P, et al. Core signaling pathways in human pancreatic cancers revealed by global genomic analyses. *Science* 2008;321:1801–6.
20. Maimaiti Y, Tan J, Liu Z, Guo Y, Yan Y, Nie X, et al. Overexpression of cofilin correlates with poor survival in breast cancer: a tissue microarray analysis. *Oncol Lett* 2017;14:2288–94.
21. Pappa KI, Lygirou V, Kontostathi G, Zoidakis J, Makridakis M, Vougas K, et al. Proteomic analysis of normal and cancer cervical cell lines reveals deregulation of cytoskeleton-associated proteins. *Cancer Genomics Proteomics* 2017;14:253–66.
22. Wang WS, Zhong HJ, Xiao DW, Huang X, Liao LD, Xie ZF, et al. The expression of CFL1 and N-WASP in esophageal squamous cell carcinoma and its correlation with clinicopathological features. *Dis Esophagus* 2010; 23:512–21.
23. Kikuchi S, Honda K, Tsuda H, Hiraoka N, Imoto I, Kosuge T, et al. Expression and gene amplification of actinin-4 in invasive ductal carcinoma of the pancreas. *Clin Cancer Res* 2008;14:5348–56.
24. Fukumoto M, Kurisu S, Yamada T, Takenawa T. alpha-Actinin-4 enhances colorectal cancer cell invasion by suppressing focal adhesion maturation. *PLoS One* 2015;10:e0120616.
25. Honda K, Yamada T, Hayashida Y, Idogawa M, Sato S, Hasegawa F, et al. Actinin-4 increases cell motility and promotes lymph node metastasis of colorectal cancer. *Gastroenterology* 2005;128:51–62.
26. Liu X, Chu KM. alpha-Actinin-4 promotes metastasis in gastric cancer. *Lab Invest* 2017;97:1084–94.
27. Shiraishi H, Fujiwara Y, Kakuya T, Tsuta K, Motoi N, Miura N, et al. Actinin-4 protein overexpression as a predictive biomarker in adjuvant chemotherapy for resected lung adenocarcinoma. *Biomark Med* 2017;11:721–31.
28. Gao Y, Li G, Sun L, He Y, Li X, Sun Z, et al. ACTN4 and the pathways associated with cell motility and adhesion contribute to the process of lung cancer metastasis to the brain. *BMC Cancer* 2015;15:277.
29. Yamaguchi H, Ito Y, Miura N, Nagamura Y, Nakabo A, Fukami K, et al. Actinin-1 and actinin-4 play essential but distinct roles in invadopodia formation by carcinoma cells. *Eur J Cell Biol* 2017.
30. Iguchi Y, Ishihara S, Uchida Y, Tajima K, Mizutani T, Kawabata K, et al. Filamin B enhances the invasiveness of cancer cells into 3D collagen matrices. *Cell Struct Funct* 2015;40:61–7.
31. Steinhardt AA, Gayyed MF, Klein AP, Dong J, Maitra A, Pan D, et al. Expression of Yes-associated protein in common solid tumors. *Hum Pathol* 2008;39:1582–9.
32. Bai H, Zhu Q, Surcel A, Luo T, Ren Y, Guan B, et al. Yes-Associated Protein impacts adherens junction assembly through regulating actin cytoskeleton organization. *Am J Physiol - Gastrointest Liver Phys* 2016; 311:G369–G411.
33. Maitra A, Adsay NV, Argani P, Iacobuzio-Donahue C, De Marzo A, Cameron JL, et al. Multicomponent analysis of the pancreatic adenocarcinoma progression model using a pancreatic intraepithelial neoplasia tissue microarray. *Mod Pathol* 2003;16:902–12.
34. Sun Q, Luo T, Ren Y, Florey O, Shirasawa S, Sasazuki T, et al. Competition between human cells by entosis. *Cell Res* 2014;24:1299–310.
35. Yang X, Cao W, Zhou J, Zhang W, Zhang X, Lin W, et al. 14–3–3zeta positive expression is associated with a poor prognosis in patients with glioblastoma. *Neurosurgery* 2011;68:932–8.
36. Tang Y, Lv P, Sun Z, Han L, Luo B, Zhou W. 14–3–3zeta up-regulates hypoxia-inducible factor-1alpha in hepatocellular carcinoma via activation of PI3K/Akt/NF-small ka, CyrillicB signal transduction pathway. *Int J Clin Exp Pathol* 2015;8:15845–53.
37. Su CH, Zhao R, Zhang F, Qu C, Chen B, Feng YH, et al. 14–3–3sigma exerts tumor-suppressor activity mediated by regulation of COP1 stability. *Cancer Res* 2011;71:884–94.
38. Tong S, Xia T, Fan K, Jiang K, Zhai W, Li JS, et al. 14–3–3zeta promotes lung cancer cell invasion by increasing the Snail protein expression through atypical protein kinase C (aPKC)/NF-kappaB signaling. *Exp Cell Res* 2016; 348:1–9.
39. Zhou Q, Kee Y-S, Poirier CC, Jelinek C, Osborne J, Divi S, et al. 14–3–3 coordinates microtubules, Rac and myosin II to control cell mechanics and cytokinesis. *Curr Biol* 2010;20:1881–9.
40. West-Foyle H, Kothari P, Osborne J, Robinson DN. 14–3–3 proteins tune non-muscle myosin II assembly. *J Biol Chem* 2018;293: 6751–61.
41. Jhaveri DT, Kim MS, Thompson ED, Huang L, Sharma R, Klein AP, et al. Using quantitative seroproteomics to identify antibody biomarkers in pancreatic cancer. *Cancer Immunol Res* 2016;4:225–33.
42. Surcel A, Ng WP, West-Foyle H, Zhu Q, Ren Y, Avery L, et al. Pharmacological activation of myosin II paralogs to correct cell mechanics defects. *Proc Natl Acad Sci U S A* 2015;112:1428–33.
43. Deng Y, Davis SP, Yang F, Paulsen KS, Kumar M, Sinnott DeVaux R, et al. Inertial microfluidic cell stretcher (iMCS): fully automated, high-throughput, and near real-time cell mechanotyping. *Small* 2017;13. doi: 10.1002/smll.201700705.
44. Effler JC, Kee YS, Berk JM, Tran MN, Iglesias PA, Robinson DN. Mitosis-specific mechanosensing and contractile-protein redistribution control cell shape. *Curr Biol* 2006;16:1962–7.
45. Kee YS, Ren Y, Dorfman D, Iijima M, Firtel RA, Iglesias PA, et al. A mechanosensory system governs myosin II accumulation in dividing cells. *Mol Biol Cell* 2012;23:1510–23.
46. Luo T, Mohan K, Srivastava V, Ren Y, Iglesias Pablo A, Robinson Douglas N. Understanding the cooperative interaction between myosin II and actin cross-linkers mediated by actin filaments during mechanosensation. *Biophys J* 2012;102:238–47.
47. Schiffhauer ES, Ren Y, Iglesias VA, Kothari P, Iglesias P, Robinson DN. Myosin IIB assembly state determines its mechanosensitive dynamics. *J Cell Biol* 2019;218:895–908.
48. Beach JR, Shao L, Remmert K, Li D, Betzig E, Hammer JA 3rd. Nonmuscle myosin II isoforms coassemble in living cells. *Curr Biol* 2014;24:1160–6.
49. Uhlen M, Zhang C, Lee S, Sjostedt E, Fagerberg L, Bidkhorji G, et al. A pathology atlas of the human cancer transcriptome. *Science* 2017; 357. doi: 10.1126/science.aan2507.
50. Wu J-Q, Pollard TD. Counting cytokinesis proteins globally and locally in fission yeast. *Science* 2005;310:310–4.
51. Robinson DN, Cavet G, Warrick HM, Spudich JA. Quantitation of the distribution and flux of myosin-II during cytokinesis. *BMC Cell Biol* 2002; 3:4.
52. Ronen D, Rosenberg MM, Shalev DE, Rosenberg M, Rotem S, Friedler A, et al. The positively charged region of the myosin IIC non-helical tailpiece promotes filament assembly. *J Biol Chem* 2010;285: 7079–86.
53. Otto O, Rosendahl P, Mietke A, Golfier S, Herold C, Klaue D, et al. Real-time deformability cytometry: on-the-fly cell mechanical phenotyping. *Nat Methods* 2015;12:199–202.
54. Reichl EM, Ren Y, Morpheus MK, Delannoy M, Effler JC, Girard KD, et al. Interactions between myosin and actin crosslinkers control cytokinesis contractility dynamics and mechanics. *Curr Biol* 2008; 18:471–80.
55. Robinson DN, Kee Y-S, Luo T, Surcel A. Understanding how dividing cells change shape. In: Egelman EH, editor. *Comprehensive biophysics*. Oxford: Academic Press; 2012. p. 48–72.
56. Liu T, Ye Y, Zhang X, Zhu A, Yang Z, Fu Y, et al. Downregulation of nonmuscle myosin IIA expression inhibits migration and invasion of gastric cancer cells via the cJun Nterminal kinase signaling pathway. *Mol Med Rep* 2016;13:1639–44.
57. Schramek D, Sandoel A, Segal JP, Beronja S, Heller E, Oristian D, et al. Direct in vivo RNAi screen unveils myosin IIa as a tumor suppressor of squamous cell carcinomas. *Science* 2014;343:309–13.
58. Conti MA, Saleh AD, Brinster LR, Cheng H, Chen Z, Cornelius S, et al. Conditional deletion of nonmuscle myosin II-A in mouse tongue epithelium results in squamous cell carcinoma. *Sci Rep* 2015;5: 14068.

Surcel et al.

59. Huelsmann S, Rintanen N, Sethi R, Brown NH, Ylanne J. Evidence for the mechanosensor function of filamin in tissue development. *Sci Rep* 2016;6: 32798.
60. Zhou X, Tian F, Sandzen J, Cao R, Flaberg E, Szekely L, et al. Filamin B deficiency in mice results in skeletal malformations and impaired microvascular development. *Proc Natl Acad Sci U S A* 2007;104: 3919–24.
61. Holterhoff CK, Saunders RH, Brito EE, Wagner DS. Sequence and expression of the zebrafish alpha-actinin gene family reveals conservation and diversification among vertebrates. *Dev Dyn* 2009;238: 2936–47.
62. Wylie SR, Chantler PD. Myosin IIC: a third molecular motor driving neuronal dynamics. *Mol Biol Cell* 2008;19:3956–68.
63. Recuenco MC, Ohmori T, Tanigawa S, Taguchi A, Fujimura S, Conti MA, et al. Nonmuscle myosin II regulates the morphogenesis of metanephric mesenchyme-derived immature nephrons. *J Am Soc Nephrol* 2015;26: 1081–91.
64. Lalwani AK, Atkin G, Li Y, Lee JY, Hillman DE, Mhatre AN. Localization in stereocilia, plasma membrane, and mitochondria suggests diverse roles for NMHC-IIa within cochlear hair cells. *Brain Res* 2008;1197:13–22.
65. Hui KL, Balagopalan L, Samelson LE, Upadhyaya A. Cytoskeletal forces during signaling activation in Jurkat T-cells. *Mol Biol Cell* 2015;26:685–95.

Cancer Research

The Journal of Cancer Research (1916–1930) | The American Journal of Cancer (1931–1940)

Targeting Mechanoresponsive Proteins in Pancreatic Cancer: 4-Hydroxyacetophenone Blocks Dissemination and Invasion by Activating MYH14

Alexandra Surcel, Eric S. Schiffhauer, Dustin G. Thomas, et al.

Cancer Res 2019;79:4665-4678. Published OnlineFirst July 29, 2019.

Updated version	Access the most recent version of this article at: doi: 10.1158/0008-5472.CAN-18-3131
Supplementary Material	Access the most recent supplemental material at: http://cancerres.aacrjournals.org/content/suppl/2019/07/27/0008-5472.CAN-18-3131.DC1

Cited articles	This article cites 59 articles, 20 of which you can access for free at: http://cancerres.aacrjournals.org/content/79/18/4665.full#ref-list-1
Citing articles	This article has been cited by 1 HighWire-hosted articles. Access the articles at: http://cancerres.aacrjournals.org/content/79/18/4665.full#related-urls

E-mail alerts	Sign up to receive free email-alerts related to this article or journal.
Reprints and Subscriptions	To order reprints of this article or to subscribe to the journal, contact the AACR Publications Department at pubs@aacr.org .
Permissions	To request permission to re-use all or part of this article, use this link http://cancerres.aacrjournals.org/content/79/18/4665 . Click on "Request Permissions" which will take you to the Copyright Clearance Center's (CCC) Rightslink site.

Targeting mechanoresponsive proteins in pancreatic cancer: 4-hydroxyacetophenone blocks dissemination and invasion by activating MYH14

Alexandra Surcel, Eric S. Schiffhauer, Dustin G. Thomas, Qingfeng Zhu, Kathleen T. DiNapoli, Maik Herbig, Oliver Otto, Hoku West-Foyle, Angela Jacobi, Martin Kräter, Katarzyna Plak, Jochen Guck, Elizabeth M. Jaffee, Pablo A. Iglesias, Robert A. Anders, Douglas N. Robinson

Supplemental Materials

Supplemental materials include following:

Supplemental Materials and Methods

Table S1. NMII Concentration (n), nM

Fig. S1. Model systems to human pancreatic cancer.

Fig. S2. Scoring analysis and differential expression patterns of mechanoresponsive and non-mechanoresponsive paralogs in patient-derived IHC data.

Fig. S3: Measurement of endogenous expression of nonmuscle myosin II paralogs and the effect of knockdown, overexpression, and 4-HAP treatment on the expression of mechanobiome proteins.

Fig. S4. Pancreatic cancer cell lines are mechanically distinct from each other.

Fig. S5: Method for quantifying actin structures at the cellular cortex.

Fig. S6: 4-HAP decreases actin retrograde flow.

Fig. S7: 4-HAP treated livers show reduced surface tumor coverage.

Movie S1. Retrograde flow of an untreated AsPC-1 Sir-Act-stained cell.

Movie S2. Retrograde flow of a 4-HAP-treated AsPC-1 Sir-Act-stained cell.

Supplemental Materials and Methods

Construct Assembly

Myosin IIC_{pep}

Using pBiEx1-mCh-IIC tail fragment construct as template, a ~100 bp PCR product for the myosin IIC_{pep} was generated using the following primers:

Forward primer: 5' – AAAAAAGTCGACAGGAACCGGCTTCGACGC – 3'

Reverse primer: 5' – TTTTATAGCGGCCGCTCATAGTCGAAGACCTG – 3'

The product was inserted into the expression construct pEGFP-N3 (Addgene), replacing the GFP, and then sequenced to verify. Then, the plasmid was transfected into cells using FuGene HD transfection reagent (Promega, Madison, WI) using 1 µg of DNA for each plasmid and imaged 36 hrs post-transfection.

Immunohistochemistry of patient-derived samples

Antibodies and reagents

Antibodies used include: myosin IIA Poly19098 (BioLegend, 909801), myosin IIB CMII 23 from the Developmental Studies Hybridoma Bank (mouse; deposited by G. Conrad and A. Conrad, Kansas State University, Manhattan, KS) used for quantitative western blots, myosin IIB (D8H8) XP (Cell Signaling Technology, #8824) used for immunohistochemistry staining of human samples, myosin IIC (D4A7) (Cell Signaling Technology, #8189), α-actinin 1 (OTI7A4) (OriGene, TA500072), α-actinin 4 (G-4) (Santa Cruz Biotechnology, sc-390205), filamin A (Cell Signaling Technology, #4762), filamin B [N1] (GeneTex, GTX101206), and β-actin (8H10D10) (Cell Signaling Technology, #3700).

Immunohistochemistry staining

Immunohistochemistry was performed as previously described (1). In short, warmed slides were deparaffinized in sequential xylene washes, followed by 100%, 95%, and 70% ethanol washes. Slides were incubated in 0.3% H₂O₂ in MeOH for 20 min, then washed twice in water. Slides are steamed in citrate buffer (pH 6.0) for 35 min. Cooled slides were washed twice in water and three times in TBST (50 mM Tris-Cl, pH 7.5; 150 mM NaCl; 0.1% Tween-20). Slides were edge

dried with a Kimwipe and Serum Free Protein Block Dako X0909 (Agilent, Santa Clara, CA) was applied for 10 min. Dried slides were incubated with primary antibody for 1 hr at 22°C, washed in TBST three times, air-dried, and incubated in secondary antibody (Dako), K400111-2, EnVision+, HRP. Mouse or K401111 -2, En Vision+ HRP. Rabbit 1100 tests (Dako) for 20 min at 22°C. Slides were washed three times in TBST, followed by incubation for 2-3 min in DAB+. Stained slides were washed with water, incubated for 15 sec in hematoxylin (Sigma), and washed first with water, then ethanol, and water again, incubated in acid alcohol, with a final water rinse. Slides are incubated in bluing water, washed, and dehydrated in 70% ethanol for 2 min, 100% ethanol for 2 min, and xylenes for 1 min.

Scoring and imaging

Slides were scanned using the Hamamatsu Digital Scanner and white balanced in Adobe Photoshop (Adobe Systems, Inc). Samples were scored based on both intensity of staining and surface area of duct covered by staining. Each slide was visualized in its entirety to determine uniformity of staining. Five cancerous ducts and five normal ducts (when present) were selected at random. Ducts with no staining were given a 0/0, ducts with intense staining on over 50% of the ductal surface were given a 2/2, with intermediate staining lying between these two endpoints. Ducts with intense staining on less than 50% of their area were scored as 2/1, ducts with moderate staining on over 50% of their ductal surface were scored as 1/2, and those with moderate staining on less than 50% of their ductal surface were scored as 1/1. To quantify the distribution of staining across all patient samples (**Fig. 2B**), individual duct scores were reassigned as follows: 0/0 as a 1, 1/1 as a 2, 1/2 as a 3, 2/1 as a 4, and 2/2 as a 5 (**Fig. S2A**). Slides were imaged on NDP.View2 NanoZoomer Digital Pathology (NDP.View2, Hamamatsu Photonics, Japan).

Quantification of cellular myosin II paralog concentrations by western analysis

Myosin II tail fragment protein purification

Bacterial expression plasmids coding for an N-terminal 6xHis tag, fused to the mCherry fluorophore, fused to the assembly domains of human myosin-IIA (residues 1722-1960), human myosin-II B (residues 1729-1976), and mouse myosin-II C (residues 1782-2033) were generated in pBiEx1 using standard cloning techniques. Proteins were expressed in BL-21 Star™ (DE3)

(Invitrogen) *E. coli* in LB shaking culture overnight at room temperature. Bacteria were harvested by centrifugation and lysed by lysozyme treatment followed by sonication, and the lysate was clarified by centrifugation. Polyethyleneimine (PEI) was added to a final concentration of 0.1% to precipitate nucleic acids, which were then removed by centrifugation. The myosin-II constructs were precipitated by adding ammonium sulfate to 50% saturation and centrifuging. The pellet was resuspended in column running buffer, dialyzed against the same for a minimum of 4 hrs, clarified by centrifugation and filtration, and run on a Ni-NTA metal affinity column, followed by a sizing column. The constructs were then concentrated and further purified by dialyzing against assembly buffer (10 mM HEPES, pH 7.1, 50 mM NaCl) until precipitate formed, followed by centrifugation and resuspension of the pellet in storage buffer (10 mM HEPES, pH 7.1, 500 mM NaCl). Protein purity was verified by SDS-PAGE followed by Coomassie Blue staining, and concentration was quantified by UV absorbance using the calculated extinction coefficient for each protein's amino acid sequence.

Quantitative western analysis

Cells were trypsinized and counted, then centrifuged into pellets containing 5×10^5 cells each. These pellets were washed in 1xPBS and recentrifuged, then lysed in 75 μ L RIPA lysis buffer plus 15 μ L 6xSDS sample buffer. Due to cell volume and residual PBS, the total lysate volume reached 100 μ L. 10 μ L of lysate was added to each well of a 7% SDS-PAGE gel, or the equivalent of 5×10^4 cells/well. In addition, each well was spiked with a known quantity of purified myosin II tail fragment, containing the epitope region for the antibodies used, with sequential 2-fold dilutions. A 7% gel was used because it allowed for optimal transfer of both the large molecular weight endogenous myosin II and the smaller molecular weight purified tail fragment out of the gel. Transfer was most effective at a constant 45V for 16 hrs, using PVDF membranes to prevent smaller protein pass-through and verifying complete transfer of larger proteins by performing a Coomassie stain to verify that no protein was left in the gel following transfer. The average volume of an individual cell for each cell type was determined from the micropipette aspiration images, where cell radius is measured, and assuming the cell shape to be a sphere prior to aspiration. For each experiment, a standard curve was created from the spiked tail fragment to determine the total number of moles of endogenous myosin II in each lane. The number of cells per lane multiplied by the average volume of a single cell gave the total cell

volume per lane, and concentration was determined as a ratio of these two values. Antibodies used were the same as those for immunohistochemistry (described above).

Quantification of myosin IIC isoforms via cQPCR

RNA was isolated from each cell line at passage number 3 using TRIzol reagent and protocol (Invitrogen). qTPCR was performed as previously described for myosin IIC isoforms (2), using Sybr green master mix for real time PCR (Applied Biosystems, Grand Island, NY). Each sample was measured in triplicate. Counts were normalized relative to GAPDH counts for each cell line. Primers for GAPDH used as a positive control were:

Forward: CATCAATGGAAATCCCATCA

Reverse: GACTCCACGACGTACTCAGC

Mammalian cell sedimentation protocol

Panc10.05 cells were trypsinized and washed in 1ml of PBS. The pellet was resuspended in 100 μ L of lysis buffer (50 mM 1,4-piperazine diethane sulfonic acid (pH 6.8), 46 mM NaCl, 2.5 mM EGTA, 1 mM MgCl₂, 1 mM ATP, 0.5% Triton X100, and protease inhibitor mixture (PMSF, N-a-tosyl-L-lysine chloromethyl ketone hydrochloride, aprotinin)). Samples were vortexed briefly and incubated on ice for 10 min, followed by centrifugation at 15,000 \times g for 5 min at 4 °C. The pellet was resuspended in 100 μ L of lysis buffer and both the pellet and supernatant fractions were passed through a qIA shredder column (QIAGEN), then heated with 2X sample buffer to 95 °C for 3 min with RNaseA. Samples were loaded on a 15% SDS/polyacrylamide gel. Western blot analyses of myosin IIC were performed.

Micropipette aspiration assay for mechanoresponse and mechanics measurements and real-time deformability cytometry measurements

The instrumental and experimental setups have been described previously (3,4). MPA assays and RT-DC measurements were all carried out in growth media for cortical tension measurements or Leibovitz L-15 media (Gibco) when fluorescence was quantified.

Measurements of mechanosensory accumulation of proteins

A pressure difference was generated by adjusting the height of a motor-driven water manometer. Mammalian cells expressing desired fluorescent proteins were loaded into the observation chamber, which was filled with Leibovitz L-15 Medium without phenol red (Gibco). Cells were deformed using a pressure of $0.3 \text{ nN}/\mu\text{m}^2$ and recorded for 5 min. Pressures higher than this often led to blebbing or the separation of cell membrane from the cortex. All cells which demonstrated blebbing during recording were discarded. Images were collected with an Olympus IX81 microscope equipped with MetaMorph software and analyzed using ImageJ (National Institutes of Health). After background correction, the fluorescence intensity at the accumulation site inside the micropipette was normalized against the opposite cortex of the cell (I_p/I_o). The peak I_p/I_o value during the 5 min timecourse was then normalized to the I_p/I_o value at $t=0$ to adjust for initial variations in cortical fluorescence (Normalized I_p/I_o).

Cortical tension measurements

Pressure was applied to the cell cortex with a micropipette (6- to $8\text{-}\mu\text{m}$ radius; R_p) to the equilibrium pressure (ΔP), where the length of the cell inside the pipette (L_p) was equal to R_p . The effective cortical tension (T_{eff}) was calculated by applying the Young–Laplace equation: $\Delta P = 2T_{\text{eff}} (1/R_p - 1/R_c)$, where R_c is the radius of the cell and ΔP is the equilibrium pressure when $L_p = R_p$ (4). Images were collected with an Olympus IX81 microscope equipped with MetaMorph software and analyzed using ImageJ (rsb.info.nih.gov/ij).

Real-time deformability cytometry

Mechanical measurements of thousands of cells were obtained as previously described (3). Approximately 10^6 cells were trypsinized, spun, resuspended in media, and incubated at 37°C for 10 min prior to loading onto the AcCellerator (Zellmechanik Dresden), using a $30\text{-}\mu\text{m}$ channel. In this device, cells are run through a microfluidic chip with a constriction channel, where the deformation and cell size data was collected in real-time at three different flow-rates and analyzed using ShapeOut 0.8.7 (Zellmechanik Dresden; available at <https://github.com/zellmechanik-dresden/ShapeOut>). Differences in deformation were plotted as a probability distribution in R (r-project.org/), and the elastic modulus, based on the median

of the deformation and area populations, the channel width, viscosity, and flow rate was calculated (5).

Imaging and Image Analysis

Imaging was performed in culture media or Leibovitz L-15 media without phenol red (Gibco) and 10% FBS for mechanoresponse and lattice light sheet experiments. Confocal imaging was performed on a Zeiss AxioObserver LSM800 microscope with a 63X (1.4 N.A.) objective (Carl Zeiss). Epifluorescence imaging was performed with an Olympus IX81 microscope using a 40X (1.3 N.A.) objective and a 1.6X optovar (Olympus), as previously described. Image analysis was performed with ImageJ (rsb.info.nih.gov/ij). Datasets were independently analyzed by multiple investigators.

Single cell assays

2D random migration

AsPC-1 cells were plated at a sub-confluent concentration in a 24-well tissue culture plate (<5,000 cells) and incubated overnight in growth media (see above). Prior to imaging, cells media was changed to Leibovitz L-15 media without phenol red (Gibco) containing 10% FBS and 1% penicillin/streptomycin. Cells were imaged using Molecular Devices IXM High Content Imager 10X objective (NA) every 30 min for 24 hrs. Cell roundness, velocity and area were quantified using ImageJ.

Retrograde flow

AsPC-1 cells were grown on collagen I-coated (50 µg/ml) 5-mm coverslips for 16 hrs and then treated with 100 nM SiR-Actin (Cytoskeleton, Inc) and 1 µM Verapamil for 4 hrs in Leibovitz L-15 without phenol red media, with or without 4-HAP (500 nM). Coverslips were transferred to the imaging chamber of the Lattice Light-Sheet Microscope (LLSM) (Intelligent Imaging Innovations) containing fresh Leibovitz L-15 media without SiR-Actin and verapamil plus the corresponding 4-HAP concentration. Cells were imaged for 3-5 min at 2-3-sec intervals, 50-150 planes per 3D stack, with a Nikon CFI75 Aplanachromat 25X/1.1 water-dipping objective. Retrograde actin flow was measured using ImageJ (rsb.info.nih.gov/ij). Datasets were independently analyzed by multiple investigators.

Transwell assays

AsPC-1 cells were plated in 6.5-mm PET membrane transwell inserts with 8- μ m pores (Costar #3464) in a 24-well plate at a concentration of 5,000 cells per well. Cells were allowed to adhere overnight in AsPC-1 media. Cell media was then changed to serum-free RPMI 1640 to starve cells for 18 hrs. Following starvation, cells were stimulated by changing media in the top chamber to fresh serum-free RPMI 1640 \pm 500 nM 4-HAP and complete AsPC-1 media \pm 500 nM 4HAP. Cells were then incubated for 24 hrs at 37°C/5% CO₂ and then fixed in 4% paraformaldehyde, permeabilized in 0.1% Triton X-100 and stained with 1 μ g/ml DAPI. Prior to imaging, the top chamber was swabbed with a cotton-tip swab and washed to remove cells that did not translocate. A total of five random fields per transwell insert were imaged using a 10X objective (NA) and number of nuclei were averaged.

Tissue spheroid generation, staining, and quantification

Tissue spheroid generation

Tissue spheroids were grown by plating Panc10.05 cells on a drop of Matrigel (Becton-Dickinson) in an 8-well slide chamber (6,500 cells per well) and grown in RPMI 1640 media (2% serum, 2% matrigel, and 10 ng/ml EGF). Spheroids were grown for 14 days with regular media changes, then aspirated off the surface of the matrigel, washed with ice-cold PBS with mild centrifugation (4,000 RCF, 5 min). For all 2D spreading assays, spheroids were then plated on 50 μ g/ml collagen-coated 8-well coverslips (MatTek) and incubated for 48 hrs in complete PANC media with 500 nM 4-HAP or PBS control. For 3D invasion assays, spheroids were resuspended in a 1.5 mg/ml collagen solution (Life Technologies) and then plated in 8-well chambered coverslips. Spheroids were incubated in complete PANC media with 500 nM 4-HAP or PBS control for 48 hrs. All spheroid samples were fixed in 4% paraformaldehyde for 15 min at 25°C and permeabilized in 0.1% Triton X-100 for 15 min at 25°C. The actin cytoskeleton was visualized with rhodamine-phalloidin (5 μ M) for 30 min. Two-dimensional spreading was visualized with Olympus Spinning disk microscope (40X oil objective, 1.3NA) or Nikon-NSIM (100X objective, 1.4NA) with an Andor EMCCD camera controlled by NIS-Elements software. Three-dimensional invasion through collagen was visualized with an Olympus Spinning Disk microscope (20X air, 0.4NA).

Spheroid cortex fluorescence quantification

Quantifications of 2D spheroids plated on a thin layer of collagen was performed using a custom-designed Matlab script (Mathworks, Natick, MA). A maximum intensity projection of 20 z-slices was extracted from each of the images and converted to 16-bit grayscale before enhancing the pixel intensity (Matlab command: `histeq`). The enhanced image was then segmented into foreground and background using the Chan-Vese method (`activecontour`), followed by filtering of small regions (`bwareaopen`), and morphological erosion (`imerode`). The boundary from this object was then obtained (`bwboundary`) and average background intensity was subtracted. This method was used for more than 80% of the images. If this boundary did not accurately reflect the shape of the spheroid, a manual tracing option was used. This option allowed the user to select a region of interest surrounding the outer edge of the spheroid (`roipoly`). Anything outside of this boundary was masked and subsequently not considered (`regionfill`). Following this, a similar binarization/background subtraction regime was implemented on the unmasked region and the boundary was traced.

For each point along the boundary, a line perpendicular to the edge was computed and the intensity along this line was used to linearize the cortex. The resultant matrix was converted into a grayscale image. The Hough Transform was used to determine the continuity of the actin belt along the edge of the cortex. Linearized cortex images were binarized using a threshold chosen to best differentiate belt from non-belt for each set of images (`imbinarize`), followed by filtering of small regions (`bwareaopen`), and morphological dilation (`imdilate`). The Hough Transform was performed on this image (`hough`), and Hough peaks and lines identified (`houghpeaks`, `houghlines`). These were used to create a continuity score defined by $(\sum \text{Hough line lengths})/(\text{number of lines} + \text{length of image})$. In this metric, higher scores indicate a more continuous actin belt at the cortex. Additionally, we computed a coarseness index of the cortex (`std2`) to describe actin distribution, the percentage of white pixels of the binarized image to characterize actin belt thickness, and the ratio of white pixels to gray pixels (greater than 0.15) to describe the distribution of fluorescence.

Mouse studies

Hemi-splenectomies

Hemi-splenectomies were performed on athymic *NCr-nu/nu* mice (Charles River Laboratories) with low passage AsPC-1 cells as previously described (6). In short, laparotomies were performed on anesthetized mice in which the upper pole of a divided spleen was reinserted into the peritoneum while 1×10^7 AsPC-1 cells prepared in phosphate buffered saline were injected into the lower splenic pole, chased by an equal volume of phosphate buffered saline. The pancreas and splenic vessels were ligated and the peritoneum was closed.

AsPC-1 cells were pretreated with 50 μ M 4-HAP or PBS 24 hr prior to injection during hemisplenectomies. Mice were also weighed and treated intraperitoneally with 200 μ l of 5 mg/ml of 4-HAP or 200 μ l PBS two days prior to surgery, and then treatment was continued every other day, starting on day 1 post-surgery. Mice were sacrificed upon spontaneous death of the first mouse. Samples from the mice of both this study and the survivability study were harvested as described below.

Livers were washed, weighed, photographed, and fixed in 10% formalin in PBS for 48 hrs, embedded in paraffin blocks, and sectioned as 4- μ m thick slides. Mice were housed and handled according to approved Institutional Animal Care and Use Committee protocol #M014M94.

Mouse liver tumor quantification

Quantifications of mouse livers were performed using a custom-designed Matlab script. RGB images were first separated into their three component channels. The imageSegmenter tool on Matlab was used to segment the individual channels identifying the area of the whole liver, the area of the tumor, and the area/location of the glare on the images, which was removed from the tumor area. The percent coverage of tumor was calculated.

References

1. Jhaveri DT, Kim MS, Thompson ED, Huang L, Sharma R, Klein AP, *et al.* Using Quantitative Seroproteomics to Identify Antibody Biomarkers in Pancreatic Cancer. *Cancer Immunol Res* **2016**;4:225-33
2. Jana SS, Kim KY, Mao J, Kawamoto S, Sellers JR, Adelstein RS. An alternatively spliced isoform of non-muscle myosin II-C is not regulated by myosin light chain phosphorylation. *J Biol Chem* **2009**;284:11563-71
3. Otto O, Rosendahl P, Mietke A, Golfier S, Herold C, Klaue D, *et al.* Real-time deformability cytometry: on-the-fly cell mechanical phenotyping. *Nat Methods* **2015**;12:199-202
4. Kee Y-S, Robinson DN. Micropipette Aspiration for Studying Cellular Mechanosensory Responses and Mechanics. *Dictyostelium Protocols II: Methods Mol Biol* **2013**;983:367-82
5. Mokbel M, Mokbel D, Mietke A, Träber N, Girardo S, Otto O, *et al.* Numerical Simulation of Real-Time Deformability Cytometry To Extract Cell Mechanical Properties. *ACS Biomater Sci Eng* **2017**
6. Soares KC, Foley K, Olino K, Leubner A, Mayo SC, Jain A, *et al.* A preclinical murine model of hepatic metastases. *J Vis Exp* **2014**:51677

Table S1. NMII Concentration (n), nM

Cell Line	NMIIA	NMIIB	NMIIC
HPDE	543 ± 73.8 (9)	46.2 ± 10.7 (8)	13.7 ± 1.55 (5)
Panc 4.03	774 ± 107 (10)*	7.10 ± 4.26 (10)**	19.9 ± 1.98 (5)*
Panc 10.05	563 ± 140 (8)	undetected (n/a)	18.0 ± 0.278 (5)*
AsPC-1	565 ± 141 (7)	undetected (n/a)	18.0 ± 1.05 (5)*
HeLa	550 ± 53.1 (10)	118 ± 4.72 (9)	undetected (n/a)

*p<0.05, **p<0.005, compared to HPDE

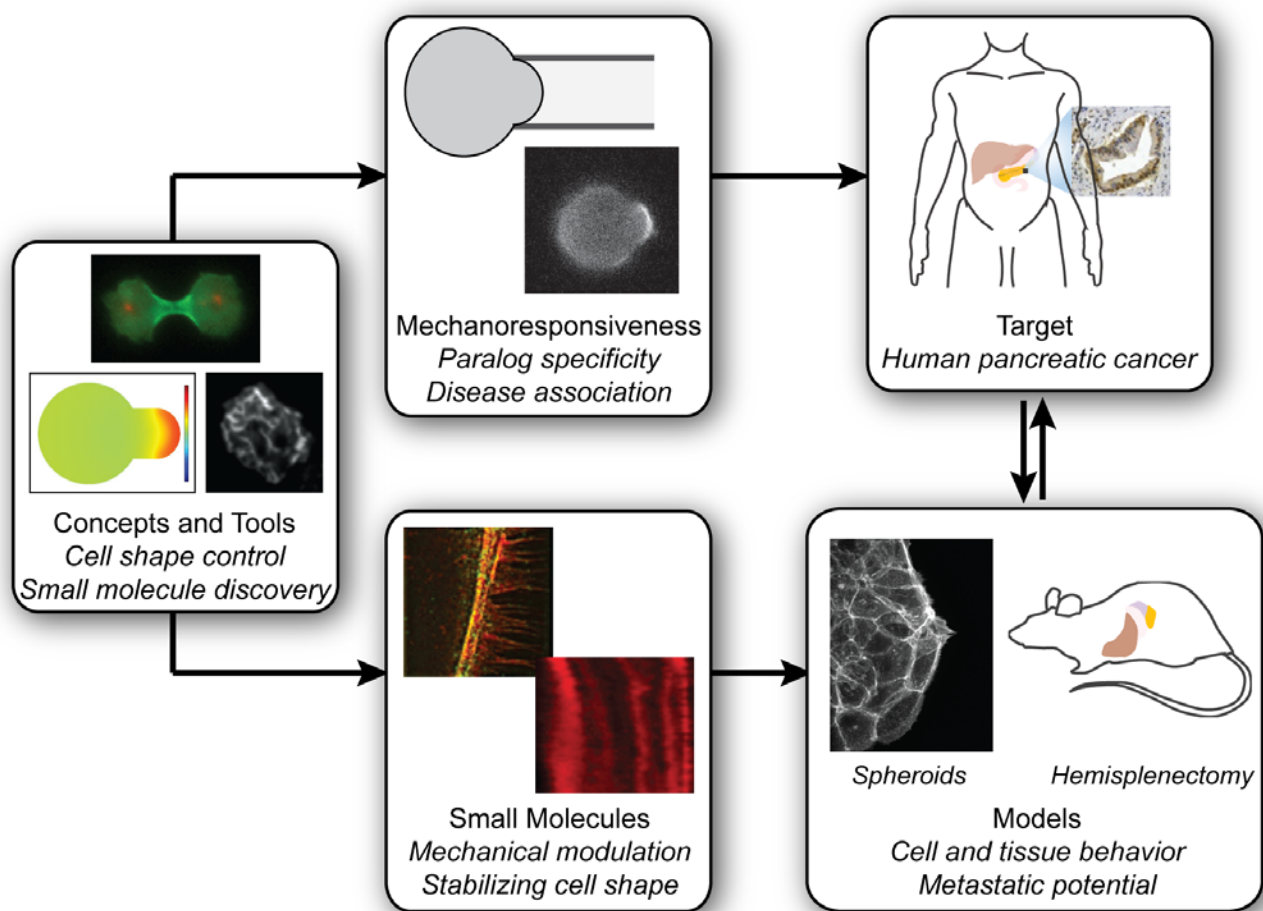


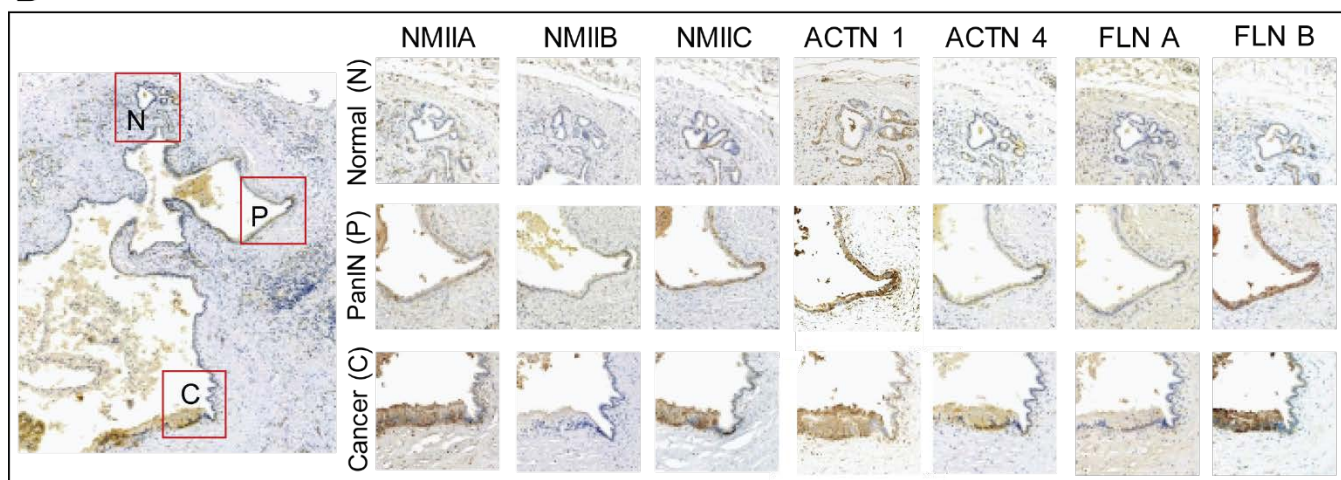
Fig. S1. Model systems to human pancreatic cancer. We have integrated our findings across models to access a targetable drug space for pancreatic ductal adenocarcinoma. We draw upon the molecular mechanisms of mechanoresponsiveness to design strategies for stabilizing the cellular dynamics that underlie metastatic potential. **Concepts and Tools:** We developed the underlying fundamental concepts for cell shape control, coupled with the identification of proteins involved in mechanical feedback regulation (mechanoresponsiveness), by studying cell division in *Dictyostelium*. This system also provided the framework for small molecule discovery used to modulate cell and tissue mechanics. **Mechanoresponsiveness:** Based on the molecular mechanisms of mechanoresponsiveness, we could predict paralog specificity of the human counterparts; those which are highly mechanoresponsive are also highly upregulated in pancreatic ductal adenocarcinoma. **Small Molecules:** A myosin II modulator 4-HAP, which we first identified in our screen using *Dictyostelium*, promotes myosin IIB and IIC assembly and

drives myosin IIC-actin transverse arcs with inhibited retrograde flow. **Models:** In human pancreatic cancer cell spheroids, 4-HAP promotes the formation of transverse actin belts, which are associated with reduced dissemination. Myosin IIA knockdown promotes increased dissemination capability, which 4-HAP can overcome. In mouse hemisplenectomy assays, 4-HAP can reduce the metastatic burden of human pancreatic cancer cells. **Target:** The goal is to decrease mortality among human pancreatic cancer patients. By combining concepts revealed in our models, which cover the dynamics, cell shape control, mechanoresponsiveness, and motility conserved in human cancer cells, we have uncovered a targetable drug space. PDAC's mechanobiome here, is targetable through the upregulation of myosin IIC and the discovery of 4-HAP, a myosin IIC modulator. Similar strategies can be employed with other elements of the mechanobiome.

A

Schematic of Ductal Intensity and Area					
Intensity/Area	0/0	1/1	1/2	2/1	2/2
Assigned Value	1	2	3	4	5
Sample Image					

B



C

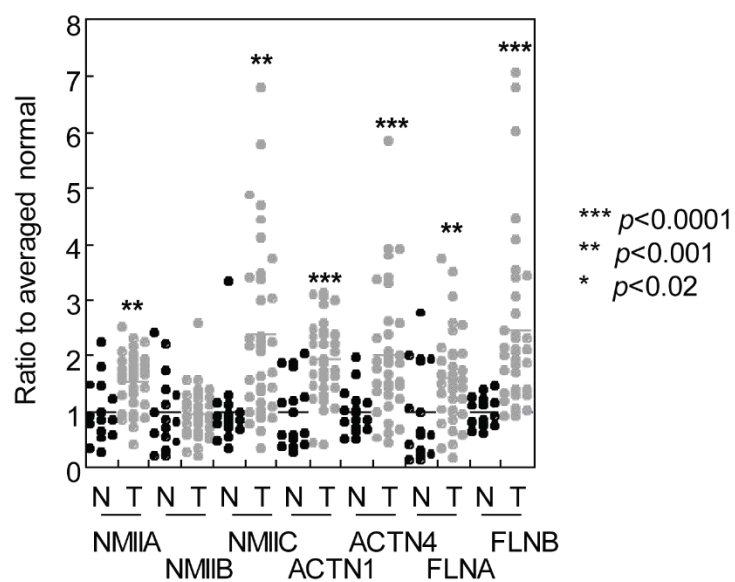


Fig. S2: Scoring analysis and differential expression patterns of mechanoresponsive and non-mechanoresponsive paralogs in patient-derived IHC data. (A) Schematic of scoring analysis of ducts from IHC data. Each analyzed duct is assigned an intensity/area value. Ducts with no staining are assigned 0/0, ducts with low intensity in less than 50% of the surface area of the duct are assigned a 1/1, ducts with low intensity staining in over 50% of the duct are given 1/2, ducts with high intensity staining in less than 50% of their surface area are assigned a 2/1, and those with high intensity in more than 50% of the duct are given a 2/2. These numbers are converted to an assigned value of 1, 2, 3, 4, and 5 respectively to be quantitatively assessed (**Fig. 2**). The sample images shown below for each assigned value are from a single patient and stained with myosin IIC antibody. (B) Sample from a duct with PanIN progression shows similar pattern of expression across all stained proteins where highly mechanoresponsive proteins (NMIIA, NMIIC, ACTN4, FLNB) increase, while non-mechanoresponsive proteins (NMIIB, FLNA) are poorly expressed or start high and remain high (ACTN1). Insets of normal (N), panIN (P), and cancerous (C) sections of the duct are presented. (C) Gene Expression Omnibus (GEO) data roughly correlates with the IHC data showing the upregulation of mechanoresponsive proteins of the PDAC mechanobiome. Normal (N) samples are compared to tumor samples (T) as normalized values to the average of the normal set within each gene. Means are provided; * $p < 0.02$, ** $p < 0.001$, *** $p < 0.0001$.

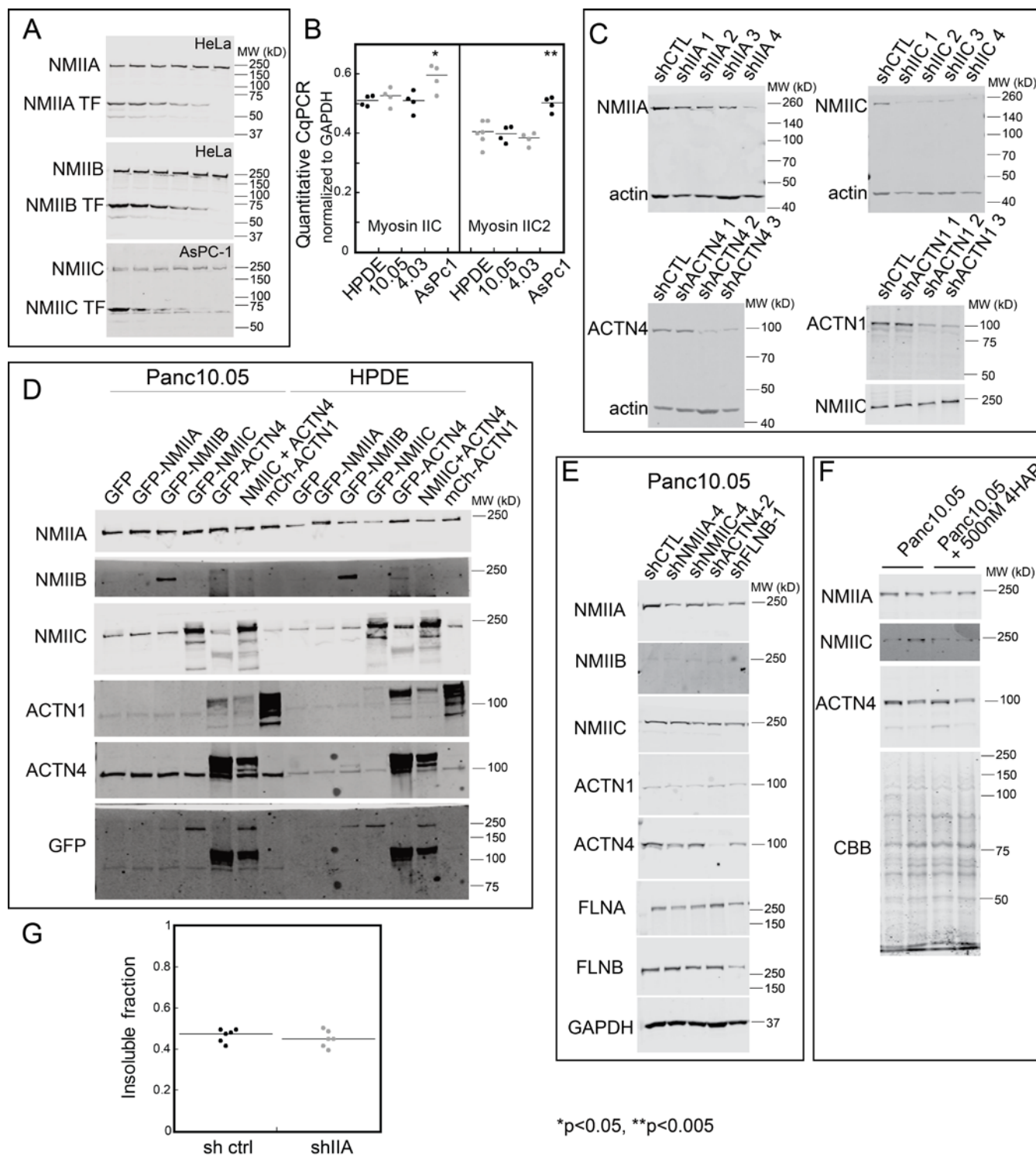


Fig. S3: Measurement of endogenous expression of nonmuscle myosin II paralogs and the effect of knockdown, overexpression, and 4-HAP treatment on the expression of mechanobiome proteins. (A) Expression of myosin IIA (NMIIA), myosin IIB (NMIIB), and myosin IIC (NMIIC) was measured by comparing endogenous expression (upper band) to a

standard curve of purified antibody epitope (lower band) added to HeLa or AsPC-1 cell extracts. **(B)** By quantitative PCR, both myosin IIC splice variants (myosin IIC and myosin IIC2) increase in expression in AsPC-1 cells. Medians are provided. **(C)** Knockdown of NMIIA, NMIIC, ACTN4, and ACTN1 using multiple shRNA constructs was confirmed by western analysis compared to a loading control (actin or NMIIC). **(D)** Overexpression of GFP-NMIIA, GFP-NMIIB, GFP-NMIIC, GFP-ACTN4, or mCherry-ACTN1 was verified by western analysis in HPDE and Panc10.05 cell lines. **(E)** Knockdown of NMIIA, NMIIC, ACTN4, and ACTN1 does not alter the expression of the other NMII and ACTN paralogs. **(F)** Overnight 4HAP treatment does not affect the expression of NMIIA, NMIIC, or ACTN4 in Panc10.05 cells (even loading verified by Coomassie Brilliant Blue staining). **(G)** Knockdown of myosin IIA (shIIA) in Panc10.05 cells did not alter the insoluble fraction (reflecting the assembled fraction) of myosin IIC. Medians are provided.

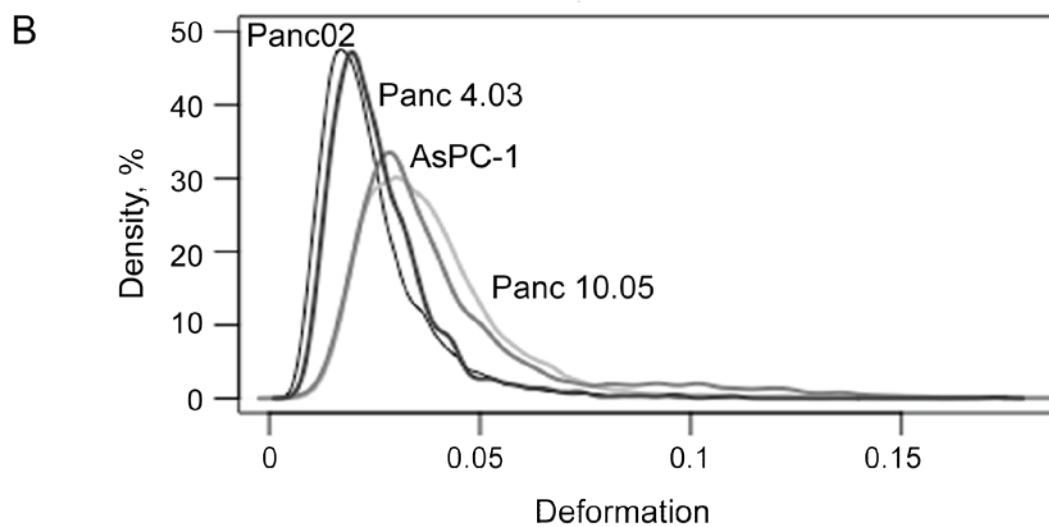
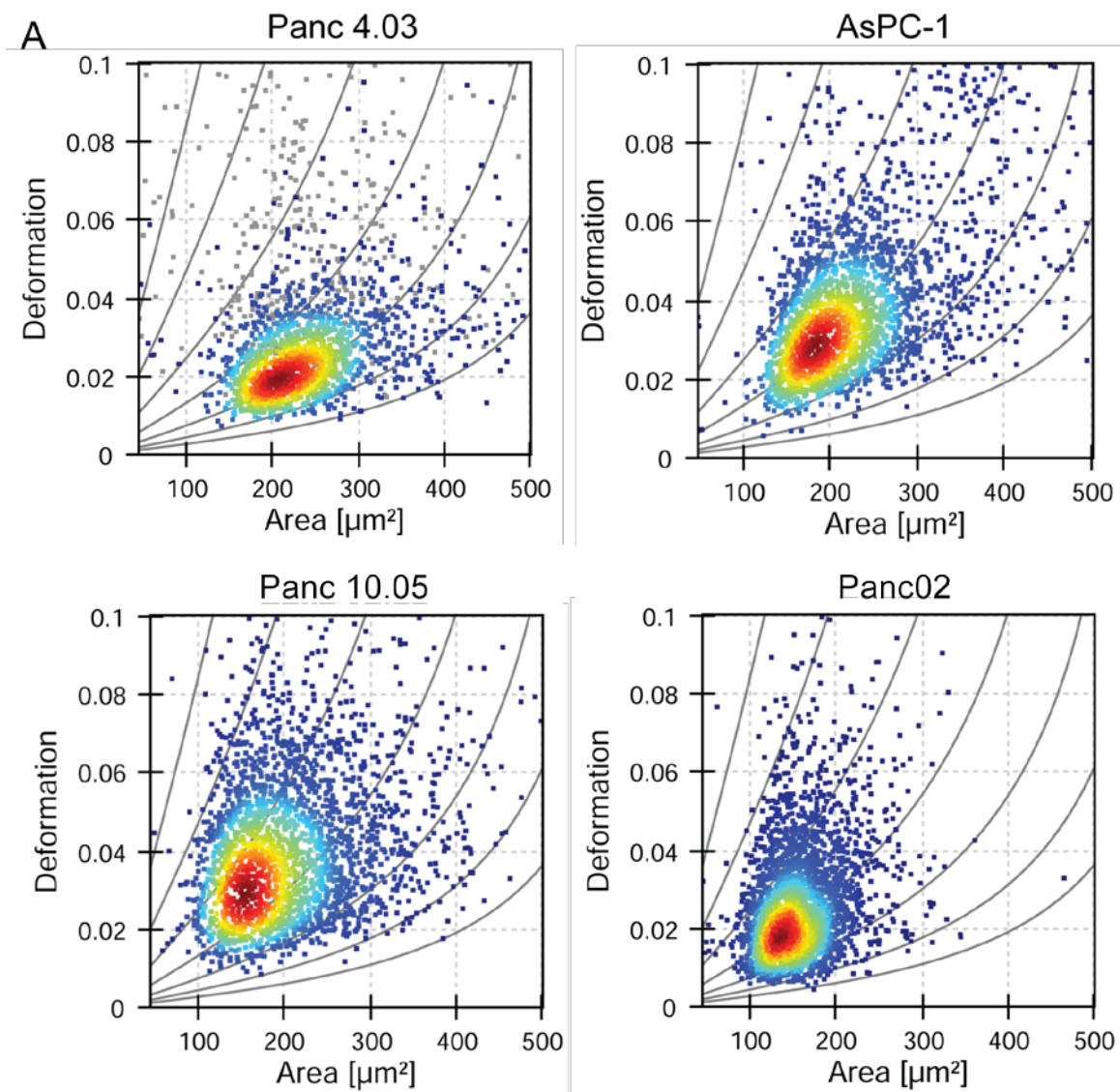


Fig. S4: Pancreatic cancer cell lines are mechanically distinct from each other. (A) RT-DC allows short-timescale cell deformation (4-ms timeframe) and cell area of thousands of cells to be rapidly measured. AsPC-1, Panc02, Panc4.03, and Panc10.05 have different degrees of deformation, likely reflecting the accumulating genetic lesions associated with the different stages of PDAC progression from which each cell-line was derived. (B) Density plots of deformation for each cell type demonstrate distinct mechanical signatures.

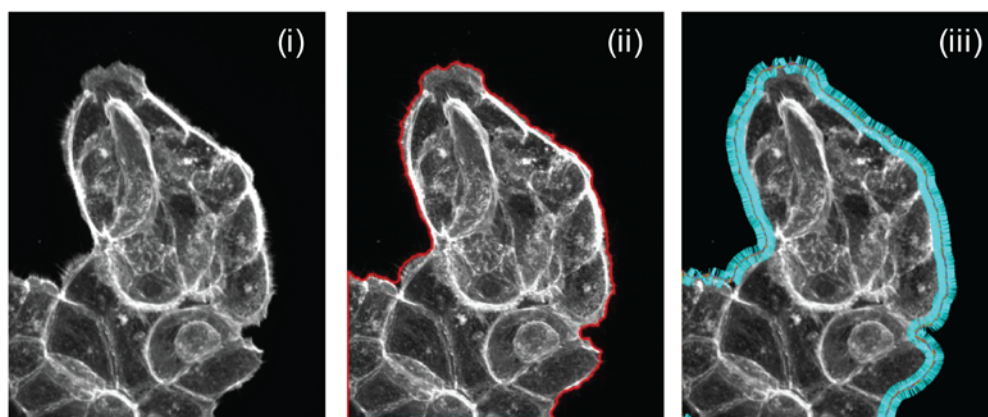
A

Steps:

Remove background (i)

Trace boundary (ii)

Draw normal lines (iii)



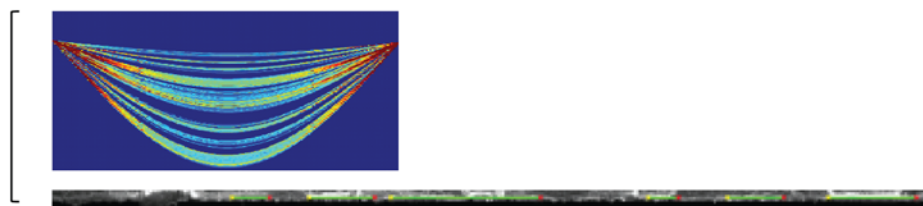
Crop the linearized boundary



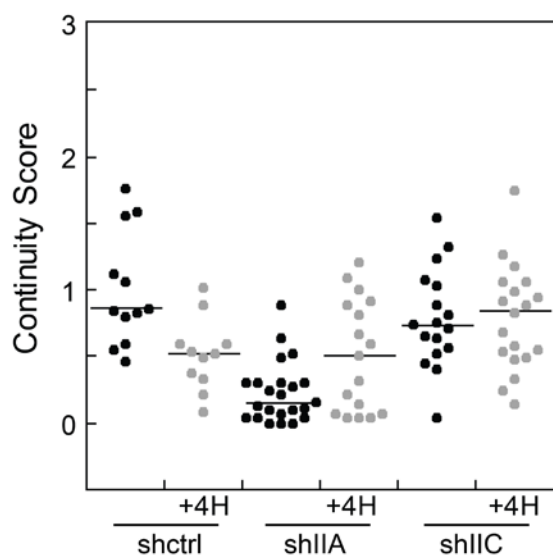
Binarize the cropped image



Hough transform to find lines



B



C

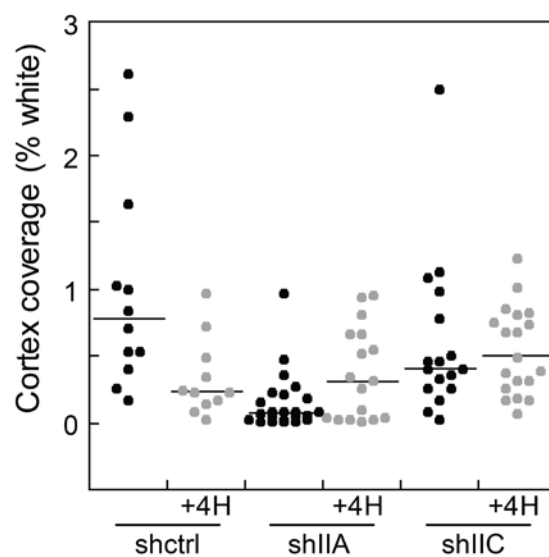


Fig. S5: Method for quantifying actin structures at the cellular cortex. (A) Sample spheroid illustrating the workflow to achieve the final linearized cortex used for quantifications. After

background subtraction (i), the edge of the spheroid was traced (ii). Normal lines were drawn from each pixel on the border (iii) to generate a linearized version of the cortex. This image was then cropped and binarized. A Hough Transform was performed on the binarized image to detect lines representing the fluorescently labeled actin bands. **(B)** From the Hough Transform we calculated a continuity score. The score is calculated by summing the lengths of the Hough lines and dividing by the number of individual Hough bands added to the length of the image. A high score indicates a more continuous actin band. The score for the control spheroids decreased upon treatment with 4-HAP, indicating an altered actin distribution upon 4-HAP treatment. The myo IIA knockdowns (shIIA) had the lowest score signifying the least continuous actin bands. Upon 4-HAP treatment, the continuity score for the shIIA cells increased significantly ($p=0.01$), indicating an increase in band continuity. The myo IIC (shIIC) knockdowns had a high score indicating a high degree of continuity, but were not affected by 4-HAP treatment indicating that 4-HAP requires myosin IIC for its action. **(C)** From the binarized cortex, additional metrics can be used to describe the cytoskeletal structure including cortex coverage defined by (number of white pixels/total number of pixels). Higher cortex coverage is roughly proportional to how much of the cortex is covered by actin bands and how thick these bands are. Control spheroids treated with 4-HAP had decreased cortex coverage, indicating an altered actin distribution. The myo IIA knockdowns had the lowest actin band coverage, but when treated with 4-HAP, the coverage increased. The myo IIC knockdowns were unaffected by the treatment of 4-HAP, but had significantly higher actin band coverage compared to the myo IIA untreated knockdowns. For B and C, medians are provided.

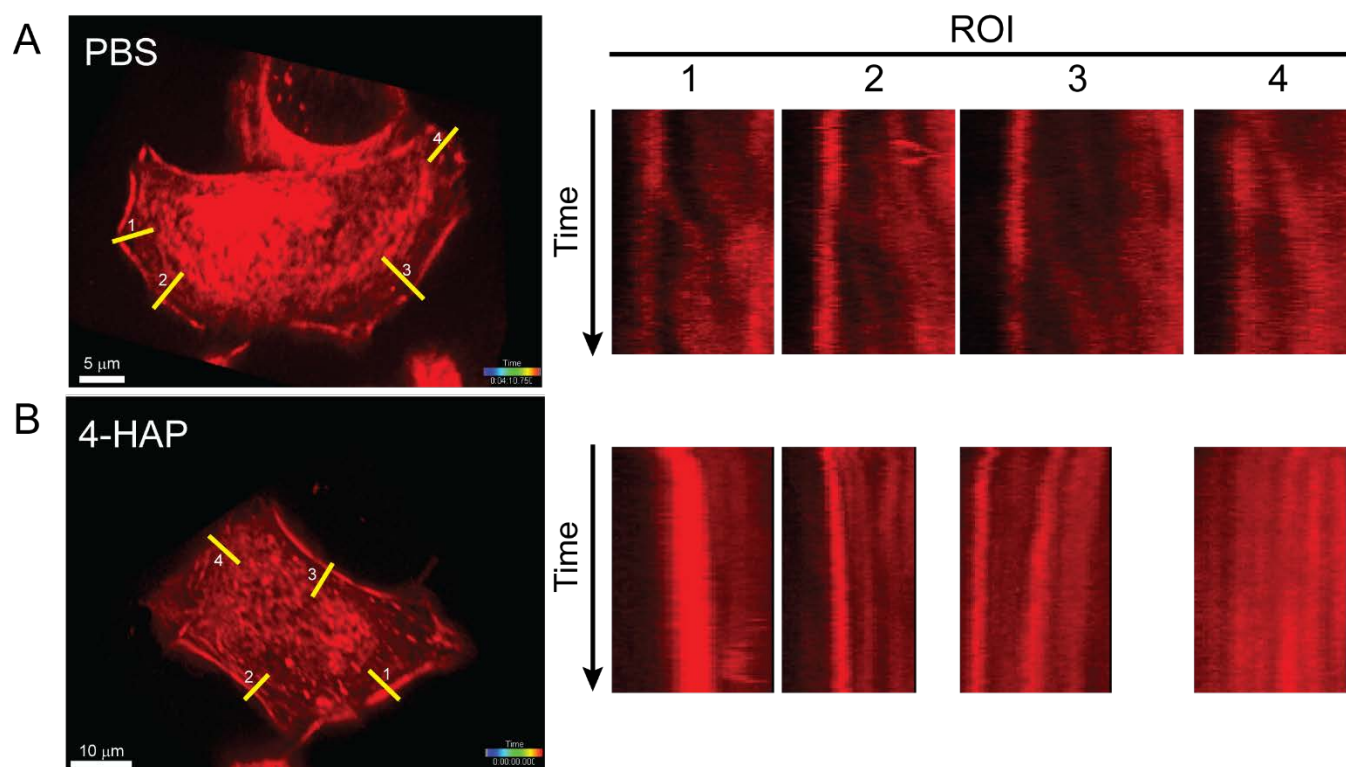


Fig. S6: 4-HAP decreases actin retrograde flow. (A) Untreated AsPC-1 cell labeled with SirAct, corresponding to **Sup. Movie 1**. (B) AsPC-1 cell treated with 4-HAP and labeled with SirAct, corresponding to **Sup. Movie 2**. Kymographs from four regions of interest (ROI) displayed on the right correspond to the four line scans (yellow) in the images on the left. Kymographs are length adjusted so that time-scale matched across the cells. Scale bars are shown on the images on the left.

A

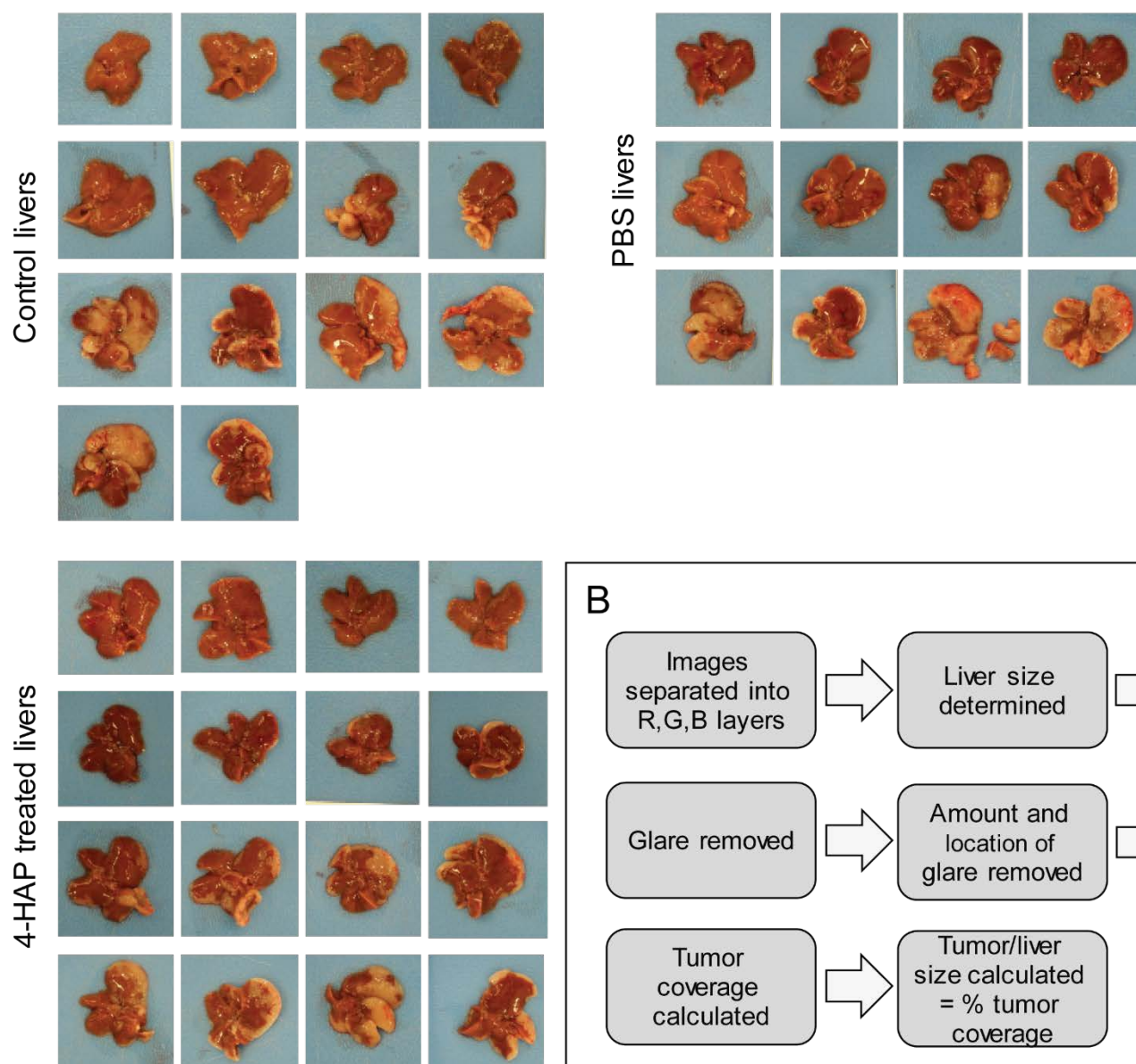


Fig. S7: 4-HAP treated livers show reduced surface tumor coverage. (A) All livers harvested from mice that underwent hemi-splenectomies are shown. (B) Work-flow diagram of quantification of tumor burden shown in main text **Fig. 6**.

Supplemental Movie Legends

Movie S1. Retrograde flow of an untreated AsPC-1 Sir-Act-stained cell. Data collected at 2.125 sec/frame; playback at 51 frames/sec.

Movie S2. Retrograde flow of a 4-HAP-treated AsPC-1 Sir-Act-stained cell. Data collected at 2.5 sec/frame; playback at 60 frames/sec.